Cell

Fast, accurate, and versatile data analysis platform for the quantification of molecular spatiotemporal signals

Graphical abstract

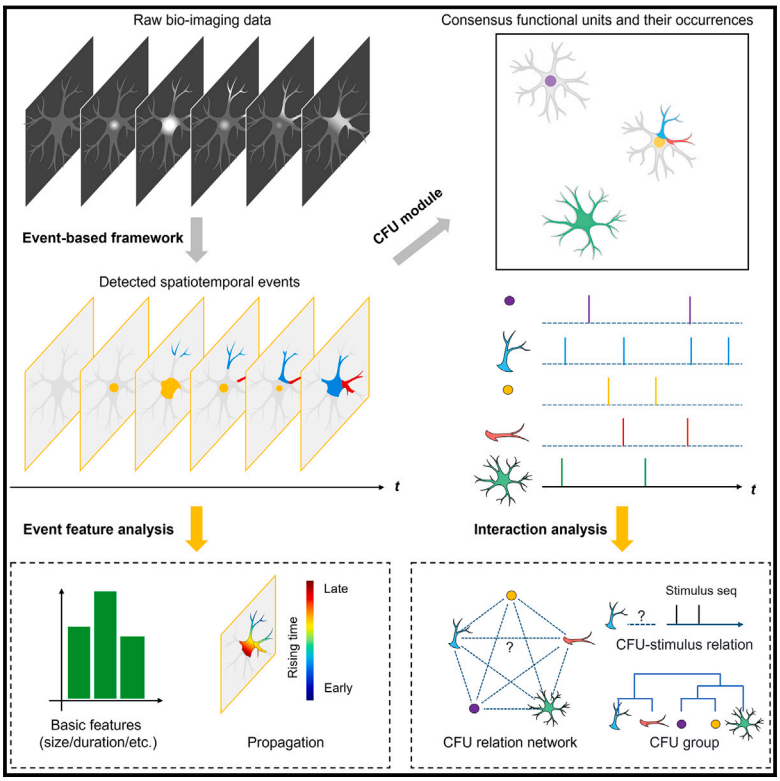

Highlights

- AQuA2 quantifies diverse subcellular-to-circuit molecular spatiotemporal signals
- Consensus functional units bridge event- and ROI-based signal detection algorithms
- AQuA2 enables fast, large-scale analysis with advanced machine-learning algorithms
- AQuA2 is open-source, supporting dual-color and 3D analysis with an intuitive GUI

Authors

Xuelong Mi, Alex Bo-Yuan Chen, Daniela Duarte, ..., Axel Nimmerjahn, Misha B. Ahrens, Guoqiang Yu

Correspondence

animmerj@salk.edu (A.N.), ahrensm@janelia.hhmi.org (M.B.A.), yug@tsinghua.edu.cn (G.Y.)

In brief

AQuA2 is a powerful data analysis platform that decomposes time-lapse imaging datasets into elementary signaling events, allowing for accurate quantification of spatiotemporal molecular activity patterns. By integrating machine learning and the consensus functional unit (CFU) framework, AQuA2 empowers scientists to detect, analyze, and visualize diverse biosensor signals across cell types, organs, and imaging techniques.

Mi et al., 2025, Cell *188*, 2794–2809
May 15, 2025
https://doi.org/10.1016/j.cell.2025.03.012

CellPress

CellPress
OPEN ACCESS

Cell

Resource

Fast, accurate, and versatile data analysis platform for the quantification of molecular spatiotemporal signals

Xuelong Mi,[1,16] Alex Bo-Yuan Chen,[2,3,4,16] Daniela Duarte,[5] Erin Carey,[5] Charlotte R. Taylor,[6,7] Philipp N. Braaker,[8] Mark Bright,[1] Rafael G. Almeida,[8] Jing-Xuan Lim,[2] Virginia M.S. Ruetten,[2,9] Yizhi Wang,[1] Mengfan Wang,[1] Weizhan Zhang,[11,12] Wei Zheng,[1] Michael E. Reitman,[6,7] Yongkang Huang,[12,13] Xiaoyu Wang,[14] Lei Li,[12,13] HanFei Deng,[14,17] Song-Hai Shi,[12,13,17] Kira E. Poskanzer,[6,7,10,17] David A. Lyons,[8,17] Axel Nimmerjahn,[5,17,*] Misha B. Ahrens,[2,17,*] and Guoqiang Yu[11,12,15,17,18,*]

[1]Bradley Department of Electrical and Computer Engineering, Virginia Polytechnic Institute and State University, Arlington, VA 22203, USA
[2]Janelia Research Campus, Howard Hughes Medical Institute, Ashburn, VA 20147, USA
[3]Department of Molecular and Cellular Biology, Harvard University, Cambridge, MA 02138, USA
[4]Graduate Program in Neuroscience, Harvard Medical School, Boston, MA 02115, USA
[5]Waitt Advanced Biophotonics Center, The Salk Institute for Biological Studies, La Jolla, CA 92037, USA
[6]Department of Biochemistry & Biophysics, University of California, San Francisco, San Francisco, CA, USA
[7]Neuroscience Graduate Program, University of California, San Francisco, San Francisco, CA, USA
[8]Centre for Discovery Brain Sciences, University of Edinburgh, Edinburgh BioQuarter, Edinburgh EH16 4SB, UK
[9]Gatsby Computational Neuroscience Unit, UCL, London W1T 4JG, UK
[10]Kavli Institute for Fundamental Neuroscience, San Francisco, CA, USA
[11]Department of Automation, Tsinghua University, Beijing 100084, China
[12]IDG/McGovern Institute for Brain Research, Tsinghua University, Beijing 100084, China
[13]New Cornerstone Science Laboratory, Tsinghua-Peking Center for Life Sciences, Beijing Frontier Research Center for Biological Structure, School of Life Sciences, Tsinghua University, Beijing 100084, China
[14]State Key Laboratory of Medical Neurobiology and MOE Frontiers Center for Brain Science, Institutes of Brain Science, Fudan University, Shanghai 200032, China
[15]Beijing National Research Center for Information Science and Technology, Beijing 100084, China
[16]These authors contributed equally
[17]Senior author
[18]Lead contact
*Correspondence: animmerj@salk.edu (A.N.), ahrensm@janelia.hhmi.org (M.B.A.), yug@tsinghua.edu.cn (G.Y.)
https://doi.org/10.1016/j.cell.2025.03.012

SUMMARY

Optical recording of intricate molecular dynamics is becoming an indispensable technique for biological studies, accelerated by the development of new or improved biosensors and microscopy technology. This creates major computational challenges to extract and quantify biologically meaningful spatiotemporal patterns embedded within complex and rich data sources, many of which cannot be captured with existing methods. Here, we introduce activity quantification and analysis (AQuA2), a fast, accurate, and versatile data analysis platform built upon advanced machine-learning techniques. It decomposes complex live-imaging-based datasets into elementary signaling events, allowing accurate and unbiased quantification of molecular activities and identification of consensus functional units. We demonstrate applications across a wide range of biosensors, cell types, organs, animal models, microscopy techniques, and imaging approaches. As exemplar findings, we show how AQuA2 identified drug-dependent interactions between neurons and astroglia, as well as distinct sensorimotor signal propagation patterns in the mouse spinal cord.

INTRODUCTION

Imaging cellular and molecular activity across space and time has emerged as a crucial approach in many fields, such as neuroscience,[1] cell biology,[2] pathology,[3] and developmental biology.[4] Recent developments in modern genetically encoded fluorescent probes[5–7] and advanced imaging techniques[8–10] have enabled the observation of a wide range of signals, including calcium ions, ATP, neurotransmitters, neuromodulators, and other molecules, greatly expanding the breadth and depth of scientific studies (Figures 1 and 2). However, with the rapid growth of data generation and the revealing of complex spatiotemporal activity patterns such as heterogeneous spatial footprints and various propagations (Figures 3, 4, and 5), quantifying and

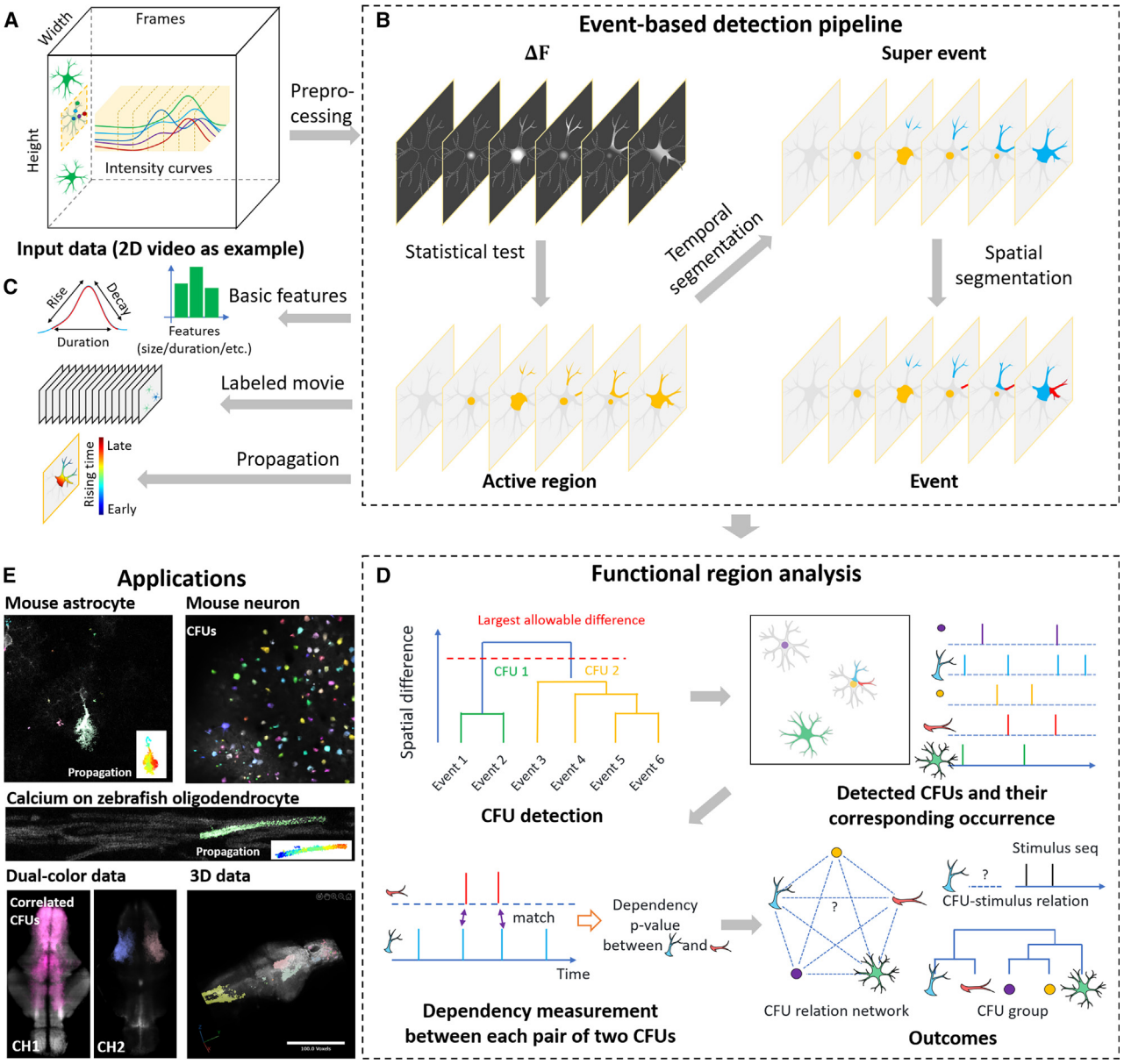

Figure 1. Flowchart and principles of AQuA2

(A) Typical input data with two spatial dimensions plus a time dimension are shown, with three exemplary cells illustrated in green. The example crop, centered around the middle cell, is utilized in (B), with intensity variations of five positions (labeled by different colors) illustrated by corresponding curves.

(B) Event-based signal detection pipeline of AQuA2, including preprocessing, active region detection, temporal segmentation, and spatial segmentation. In the outcome of each step, different colors indicate that the corresponding pixels/regions belong to different detection results.

(C) Potential outputs based on event detection pipeline, including extracted event features (spatial footprint shape and size, temporal duration and magnitude, etc.), movie with events overlaid and propagation map.

(D) Diagram for functional region analysis. It consists of consensus functional unit (CFU) detection (cluster events with similar spatial patterns) and interaction analysis between CFUs (take event occurrence sequence as input, output significance *p*-value of dependency). The outcomes include CFU interaction network, CFU-stimulus relationship, and CFU groups.

(E) Example applications of AQuA2, including signals of different cell types, different biosensors, dual-color data, and 3D data.

See more diagrams, illustrations, and 3D implementation in Figures S1, S2, and S3.

understanding the data have become a limiting factor. Manual inspection is simply infeasible owing to the complexity of data and large data size, and even when possible, it often misses subtle yet important information. Although automated image analysis methods have been developed, they are typically constrained to modeling a specific type of signal with an assumption of a simple spatiotemporal pattern or are plagued by low accuracy, extensive processing times, and a limited set of analysis functions, failing to

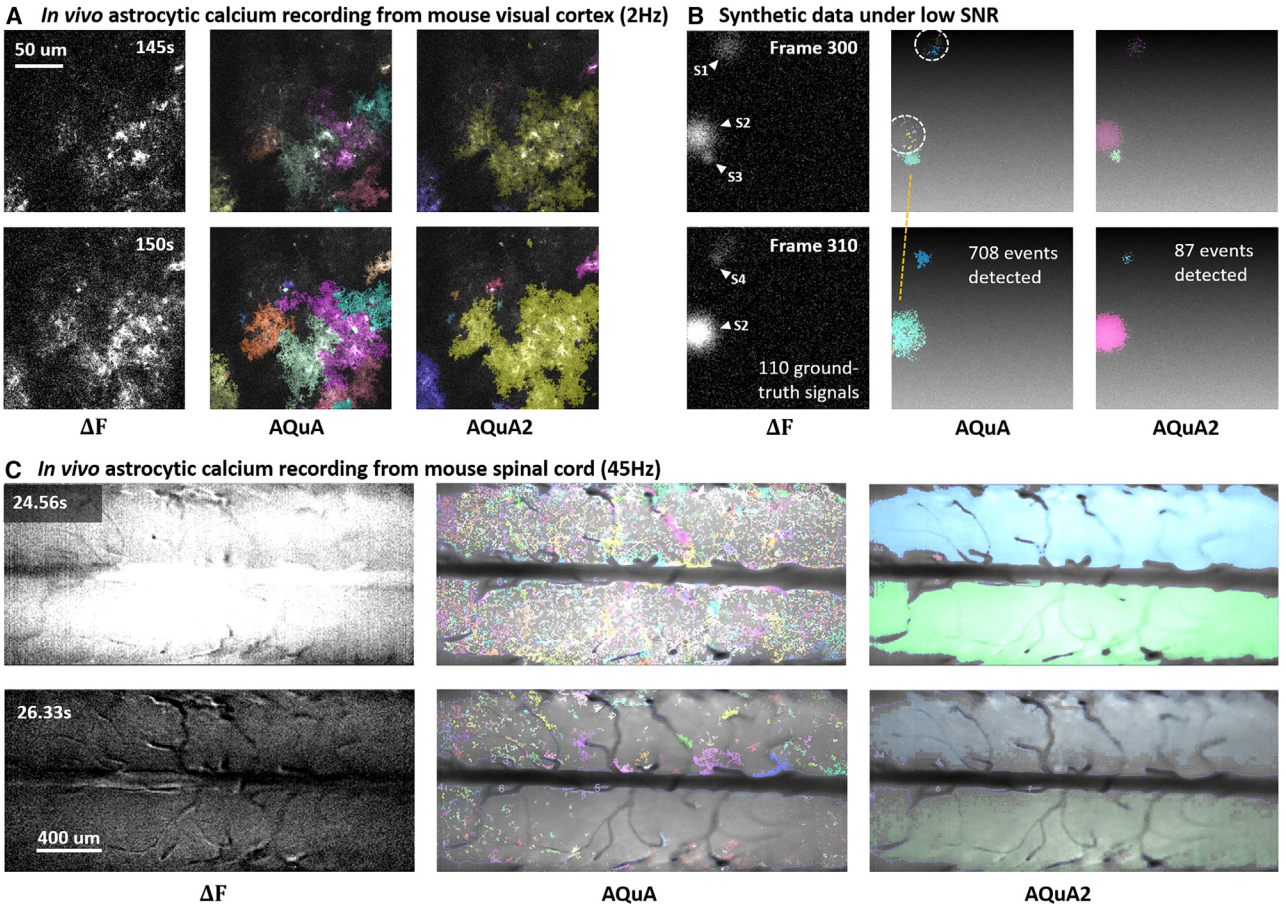

Figure 2. AQuA2 improves the accuracy of AQuA

(A) Performance comparison between AQuA and AQuA2 on a two-photon *in vivo* astrocyte calcium recording from the primary visual cortex (V1) of awake, head-fixed mice (recorded at 2 Hz), which was used as a test example in the AQuA paper. The selected time point is during a signal burst period. Both AQuA2 and AQuA successfully detect the signal burst, but AQuA2 identifies the burst as a unified entity, providing a more intuitive representation.

(B) Performance comparison on a synthetic dataset comprising large and small signals under a significantly low SNR. Among the 110 ground-truth signals, AQuA2 detects 102 and AQuA detects 105. AQuA2 generates 0 false positives, while AQuA produces 734 false positives. White triangles label the ground-truth events in the present time points. Erroneous detections are marked by white dashed circles.

(C) Performance comparison on a miniature one-photon astrocyte calcium recording from the mouse spinal cord (recorded at 45 Hz). During detection, a mask is applied to mitigate the influence of blood vessels. In the AQuA and AQuA2 detection results, each colored region presents one detected signal event. Many parts in the big events were either missed or falsely split by AQuA into numerous fragments.

See also Videos S1, S2, and S3.

meet today's demands for a unified data analysis platform that allows flexible and accurate quantification of diverse and complex data from various experimental settings.

In the context of activity quantification, existing fluorescent imaging analysis techniques can be roughly grouped into two categories: region-of-interest-based (ROI-based) methods[11–13] and event-based methods.[14–16] ROI-based methods, such as suite2p[12] and CaImAn,[11] rely on identifying ROIs, which are ill-suited to capture the spatial dynamics of molecular signals. An ROI is a fixed spatial area associated with a single temporal dynamic. While certain ROI methods, such as non-negative matrix factorization (NMF)-based approaches,[11,17] permit overlap between regions, they are based on weighted averages of a low number of temporal components and do not allow for the spatial dynamics to be faithfully captured. These methods can be effective for analyzing stereotypical somatic or nuclear neuronal signals. However, their stringent assumption of spatial stationarity often results in suboptimal performance and frequently distorted quantification when the target signals exhibit complex and flexible spatiotemporal dynamics. Event-based methods, in contrast, are specifically designed to capture dynamic activities with intricate spatiotemporal features. Astrocyte quantitative analysis (AQuA),[14] developed by our team and widely used in the astrocyte field, pioneered event-based quantification. Because events are jointly determined by the spatial coherence and the temporal pattern, it allows for more flexible modeling of both spatial and temporal dynamics than traditional ROI-based models, in that one pixel can participate in different kinds of

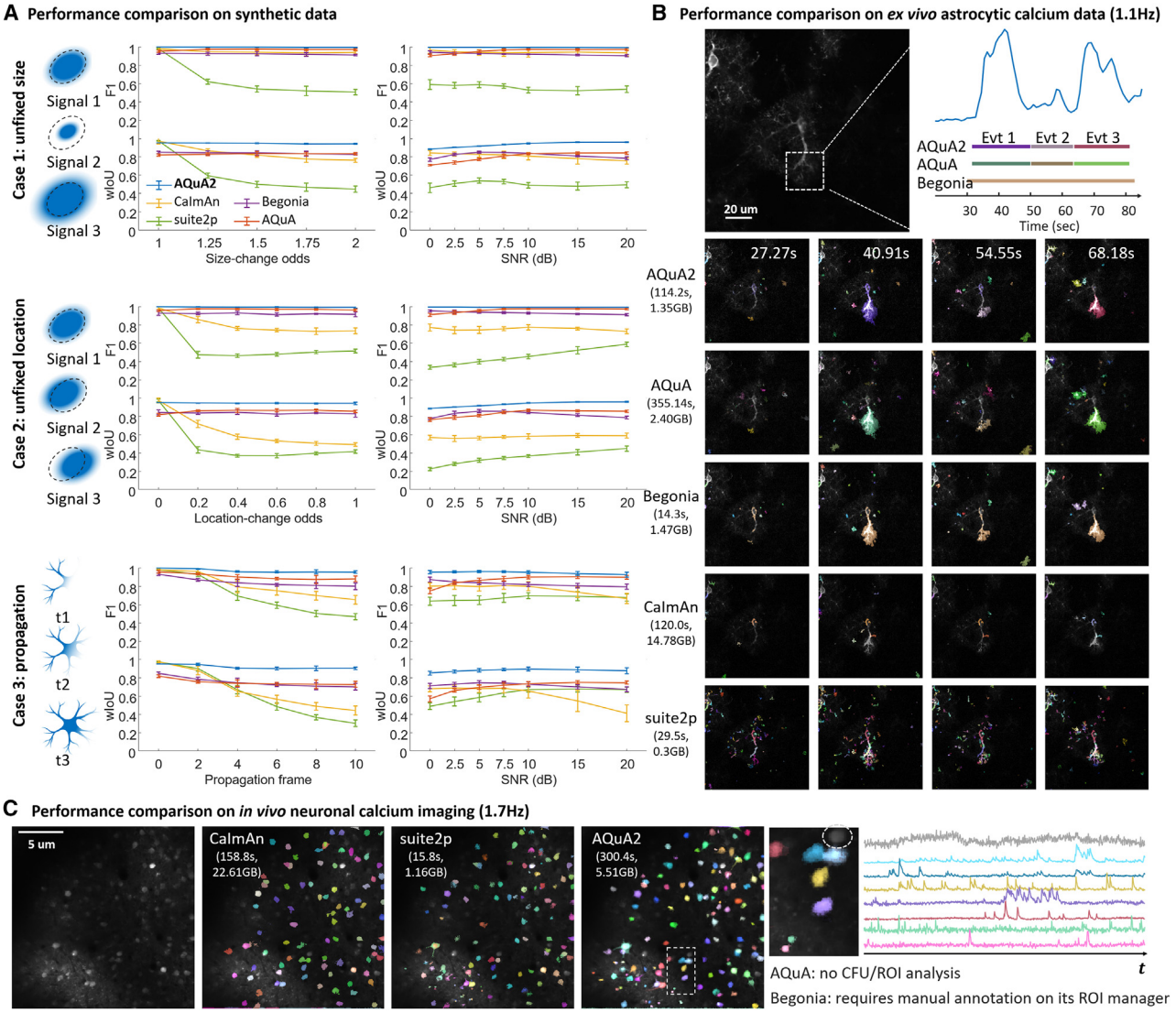

Figure 3. AQuA2 outperforms peer methods (suite2p, CaImAn, AQuA, and Begonia) on both synthetic and real datasets

(A) Performance (F1 score and wIoU measure, see STAR Methods) comparison between AQuA2 and peer methods under scenarios of unfixed size, unfixed location, and propagation. Left column: illustration of signal variations. Middle column: performance comparison under different levels of signal variation with SNR fixed to 10 dB. Right column: performance comparison under different SNRs with a moderate signal variation. For all results, we used mean ± 2 × standard deviation, derived from 12 independent replications of evaluation. See more comparison in Figure S4.

(B) Performance comparison on *ex vivo* astrocytic *GCaMP6f* calcium imaging in a mouse brain slice.[14] Each colored region indicates one detected event. A white dashed box highlights the major signals of interest, and its average curve is shown on the right. The time intervals of detected signals by the event-based methods are marked with line segments in corresponding colors. Begonia over-merged three events into a single one; CaImAn missed several key signals; and suite2p over-segmented the signals into numerous fragments.

(C) Performance comparison on *in vivo* neuronal *GCaMP6f* calcium imaging data from the mouse visual cortex. Each colored region indicates one identified CFU or ROI. Example CFUs identified by AQuA2 in white dashed box, and their corresponding activity curves are shown in the right subfigure, with one silent neuron manually labeled in gray. Small regions were also detected by AQuA2, which may be related to repeated dendritic signals. Since AQuA and Begonia cannot perform CFU or ROI analysis, no results are shown here.

See also Figure S4.

events, and any one signal can propagate across space. This makes AQuA widely adopted for quantifying astrocyte calcium signals that can flow along the geometry of the cell and exhibit subcellular and population-wide spatial dynamics.

With growing AQuA usage,[18–21] we, as its developer, have received numerous requests for a fast, accurate, and versatile platform with more functions to enhance the quantification and analysis of generic molecular spatiotemporal activity. First, researchers find region or location information helpful in interpreting their results, and therefore, they need analysis methods that integrate region-based and event-based approaches. Second, as multiplexing imaging methods are maturing,[22,23]

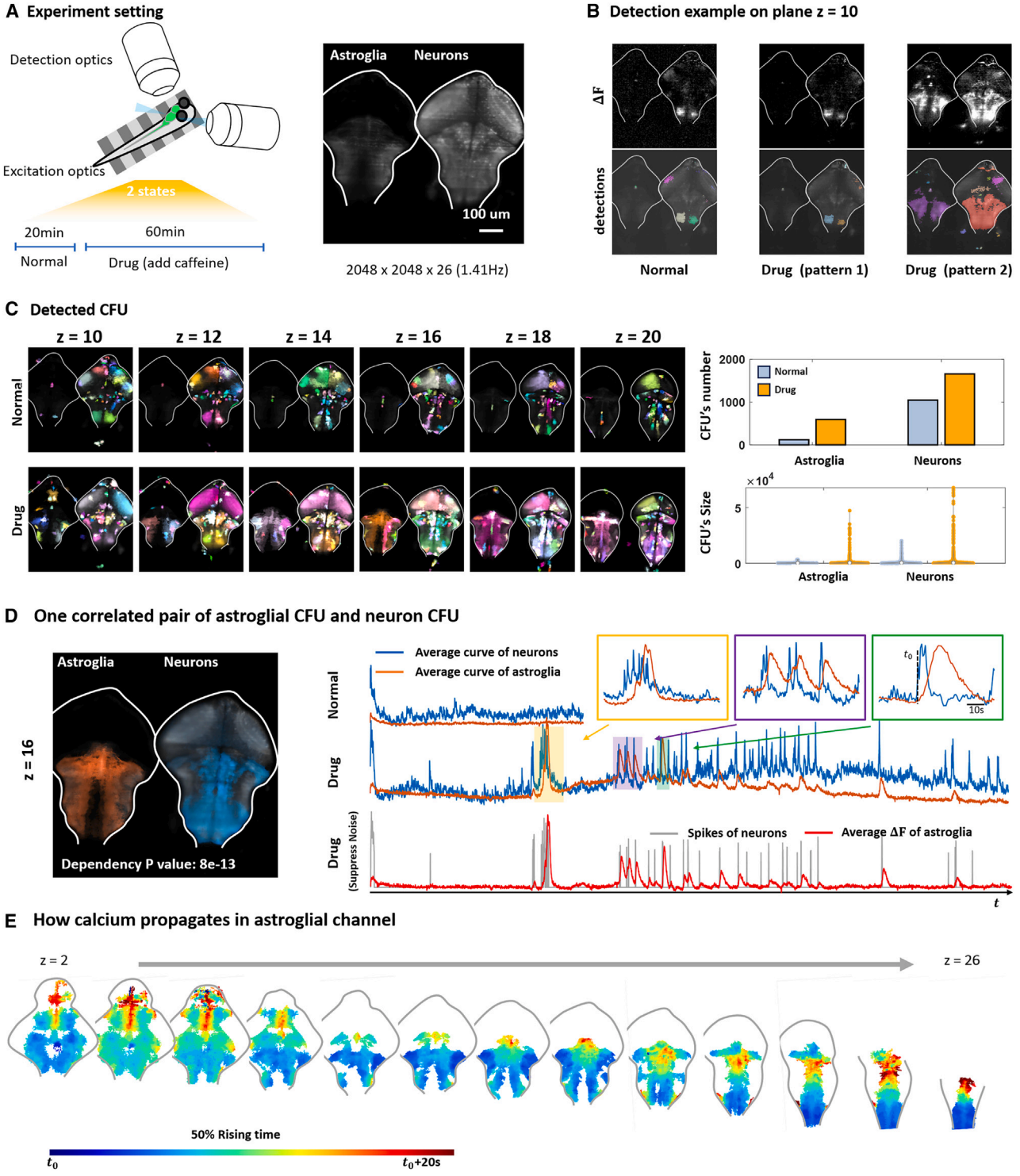

Figure 4. AQuA2 identifies the signal pattern changes in zebrafish astroglia and neurons under the addition of caffeine and reveals the correlation between these two cell types

(A) The experiment setting and average projection of the data. Zebrafish were engaged in fictive swimming in a virtual-reality (VR) environment with realistic visual feedback during swimming, recorded by a light-sheet microscope. Experiments of two distinct states were conducted: normal state and under the influence of caffeine (drug state). Astroglia calcium (left) and neuronal calcium (right) were expressed using *Tg(ELAVL3: GCaMP7f; GFAP: jRGECO1B)*.

(B) Visualization of Δ*F* and AQuA2 detection results for the different states. Each colored region represents one detected event. Two distinct signal patterns are found in the drug state, where pattern 1 mirrors neuronal signal in the normal state, and pattern 2 is composed of drug-state-specific astrocytic signal.

(legend continued on next page)

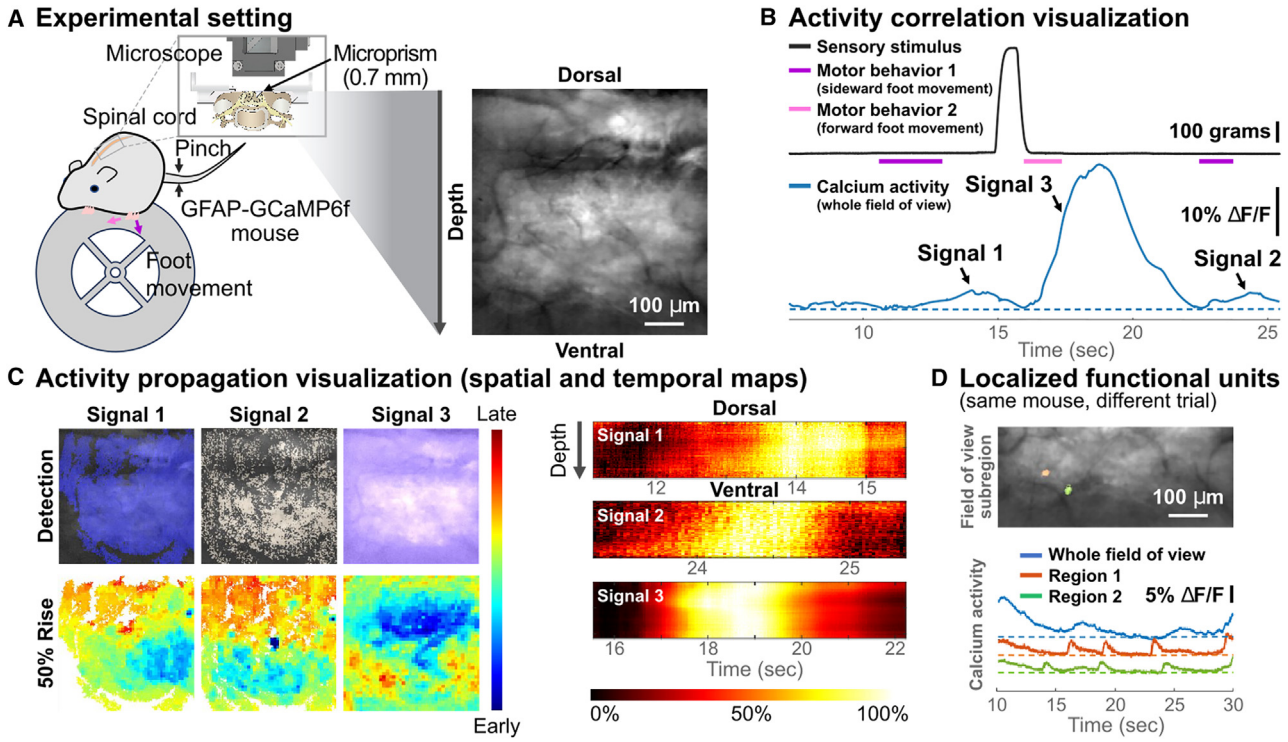

Figure 5. AQuA2 unveils differences in signal propagation of sensory- and motor-evoked astrocyte calcium signals in the mouse spinal cord

(A) Experimental setting: miniature one-photon translaminar imaging[8] was performed in the lumbar dorsal horn of an awake behaving *Tg(GFAP:GCaMP6f)* mouse on a spherical treadmill. A pressure stimulus was applied to the mouse's proximal tail.

(B) Temporal relationship between the applied sensory stimulus (tail pinch; black), mouse motor behavior (sideward and forward foot movements; purple and pink, respectively), and the average calcium activity across the field of view (blue).

(C) Spatial (left) and temporal (right) activity propagation maps of the three signals indicated in (B). The color spectrum depicts earlier activation in blue and later rising times in red. The sensory-evoked signal (3) displayed a propagation pattern starting from the dorsal side, while the motor-evoked signals (1 and 2) emanated from the ventral side.

(D) Detected localized functional units (orange and green; top) and their corresponding calcium transients (bottom).

there is a need to model more than one type of signal and analyze the interactions between them. Third, since scientists aim to minimize the disturbance to the system under investigation, datasets with low signal-to-noise ratios (SNRs) are generated, requiring more accurate algorithms to cope with large noise. Fourth, new data are getting larger and larger, frequently involving three spatial dimensions. The large data size necessitates better approaches in terms of both computational time and computer memory. Finally, although AQuA was originally designed primarily for astrocyte calcium activity, it has been applied to many other cell types and signals without thorough validation and optimization.

Responding to the feedback and requests, we developed activity quantification and analysis (AQuA2), an improved version of AQuA. Now, the first letter A in AQuA2 stands for activity instead of astrocyte as in AQuA, indicating the great expansion of applicability. We introduce the consensus functional unit (CFU)concept to integrate the ROI-based and event-based approaches. Potential functional units, termed CFUs, are detected with the hypothesis that a functional unit is expected to exhibit multiple events with a consistent spatial footprint/region. The CFU concept, bridging region and event definitions, can be considered a more flexible version of ROI, allowing signals to have different sizes, shapes, and propagation patterns while maintaining consistent spatial foundations. This function can facilitate deeper biological insights by utilizing strengths from both ROI-based and event-based approaches. Moreover, introducing CFUs enables us to analyze the interaction between signals recorded by different biosensors. To improve the accuracy when used on noisy data, we designed a more reliable top-down strategy, which utilizes more

(C) Left: detected CFUs across different planes under two states. Each colored region represents one extracted CFU. Right: comparison of number and size among identified CFUs in the two states.

(D) The most correlated pair of astroglial CFU and neuronal CFU on one plane, with their curves drawn on the right. Zoomed-in traces of three time windows (yellow, purple, green) are also given. For the curves of drug state, neuronal spikes (gray) are additionally extracted (by suppressing small fluctuations on ΔF) and compared with the average ΔF of astroglia (red).

(E) Propagation pattern of the astroglial calcium signal on different planes. The blue color shows the earliest rising time, while the red color shows the latest rising time.

information from a broader field of view (FOV) than the original bottom-up approach. This strategy integrates principles of probability theory while adopting innovative machine-learning algorithms such as bidirectional pushing with linear component operations (BILCO)[24] for ever-growing data volumes. It can efficiently and accurately quantify signals with various features. Furthermore, to enhance usability, we have equipped AQuA2 with a user-friendly interface compatible with processing two-dimensional (2D), three-dimensional (3D), and dual-color data.

AQuA2 surpasses existing ROI- and event-based methods (suite2p,[12] CaImAn,[11] Begonia,[16] and AQuA[14]) in accuracy and demonstrates high efficiency, corroborated through extensive testing on both simulated and real-world data. Many additional signal properties, such as the potential functional units, the interaction between signals, and 3D signal propagation, can be readily captured by AQuA2 but are difficult or impossible to capture with existing methods, individually or combined. The user interface is optimized so that the operation is intuitive, and detection parameters can be set based on known biological constraints. Using AQuA2, we quantified the dynamics of several distinct biological signals, including calcium, norepinephrine (NE),[5] dopamine,[25] ATP,[6] and acetylcholine (Ach).[26] Our study involved various cell types (neurons, astrocytes, microglia, and oligodendrocytes), organs (brains and spinal cords), animal models (mouse and zebrafish), microscopy techniques (confocal, one-photon, two-photon, light sheet), and imaging approaches (single session or multiple sessions). Additionally, using AQuA2, we explored drug-dependent interactions between neurons and astroglia and discovered different modes of sensorimotor signal propagation in the mouse spinal cord. These results establish AQuA2 as a broadly applicable toolkit capable of addressing a wide array of scientific inquiries.

RESULTS

Event detection pipeline of AQuA2

The event-based methodology, first introduced in AQuA,[14] provides a unique perspective for modeling spatiotemporal activities. It defined an event as a spatiotemporally connected region characterized by fluorescent dynamics, containing a single temporal peak pattern, and originating from a single source. Adjacent pixels belonging to the same event are allowed to exhibit slight delay or deformation in temporal patterns, empowering the analysis of signals with complex features. In AQuA2, we have retained this concept but enhanced the reliability of the event detection pipeline by adopting a top-down framework that incorporates advanced machine-learning algorithms. It obtains the signal events by segmenting regions with significant dynamics in the following steps, as depicted in Figure 1B: (1) baseline estimation and change in fluorescence (ΔF) calculation according to the non-negative nature of dynamic signals, (2) active region detection by applying statistical tests on ΔF, (3) temporal segmentation through machine-learning and image processing techniques to ensure that each segmentation (super event) contains a single temporal peak pattern, and (4) spatial segmentation based on the signal propagation estimated using joint alignment techniques to ensure that each final event originates from a single source. For a more detailed explanation of each step, please refer to STAR Methods.

The proposed pipeline, in contrast to AQuA, demonstrates superior accuracy and efficiency owing to key enhancements. First, AQuA2 adopts a top-down framework, which is intrinsically more robust, compared with the bottom-up framework used in AQuA. The bottom-up framework, designed to aggregate voxels into events, tends to place excessive emphasis on the temporal information of individual pixels. This makes it susceptible to noise interference, especially in low SNR environments. By contrast, the top-down approach, which identifies signal events by segmenting potential active regions, achieves better performance by integrating the information carried by all the voxels in a broader scope. Combined with the flexibility of event-based methods, this improvement enables AQuA2 to robustly capture a wide range of molecular spatiotemporal activities across various experimental setups. Second, by developing and applying advanced machine-learning techniques, we made technical innovations in almost every component of the pipeline to achieve accurate analysis with low SNR. These efforts include the development of innovative methods for baseline fluorescence estimation, noise level estimation, peak detection, integration of prior knowledge, multiscale usage of spatial compactness, split of super-events, and removal of technical artifacts (see STAR Methods). Third, AQuA2 has optimized efficiency by incorporating an innovative machine-learning algorithm called BILCO.[24] This algorithm was specifically designed to address the most computationally intensive module, which accounts for approximately 70% processing time of the whole pipeline and the bottleneck for memory consumption in the original version of AQuA. As a result, there is an average 10-fold improvement in both runtime and memory usage in this module. It leads to a more than 2-fold acceleration of the entire pipeline, compared with AQuA without BILCO, and its efficient memory usage enables the application on 10-fold larger data.

Identifying CFUs and interaction analysis

In response to the limitations of event-based methodologies, which treat individual events as isolated outcomes and are ignorant to the significance of regions with repetitive signals, we introduced the CFU concept and developed the CFU module as an integral component of AQuA2. We hypothesized that if one spatial region generates repeated signal events, it is more likely to be a functional unit, and we refer to such a region as a CFU. This concept offers greater flexibility, compared with ROIs, allowing each occurrence of signals to have different sizes, shapes, and propagation patterns while maintaining consistent spatial foundations. CFUs can represent various entities, including cellular compartments, individual cells, cell clusters, tissues, and even entire organs, depending on the data type or scope of recording.

Based on this assumption, we have employed a hierarchical clustering algorithm to identify CFUs by grouping signals with similar spatial patterns, as shown in Figure 1D. The CFU behind each group can be represented by the average spatial pattern, while the onset time of these signals creates a corresponding event occurrence sequence. This sequence can facilitate the exploration of the interrelationships between CFUs. Compared with the classic ROI-based methods that rely on NMF[27] or similar approaches, our CFU identification offers several distinct

advantages: First, it inherits the flexibility of the event detection pipeline. Even when signals from the same source exhibit varying sizes, subtle location changes, or propagations, our approach can adeptly capture the underlying functional unit. By contrast, ROI-based methods may segment the regions into several arbitrary parts under such conditions (see Figure S4). Second, unlike the notoriously hard problem of determining the number of components in ROI-based methods, the CFU module prompts users to set a parameter for the similarity of spatial signal patterns, fostering a more intuitive approach to clustering signals together. Third, CFU identification does not have any bias toward the size of detected components. By contrast, NMF-based methods tend to favor larger components to minimize errors and ignore small functional units.

We have also developed a statistical approach for analyzing interactions among identified CFUs. This approach takes sequences of event occurrences in CFUs as its input and assesses the significance of dependency between any pair of CFUs (see STAR Methods). Compared with traditional methods using correlation, it effectively mitigates the confounding influence of signal shape and duration, enabling precise measurement of interactions among CFUs displaying entirely different signal forms. The interaction analysis, sometimes also called network analysis, is particularly useful when multiple measures are available. For instance, in dual-color neuron and glial data, this approach can discover the associations between neuronal cells and glia, while traditional correlation analysis would fail due to the mismatch of the temporal characteristics of (calcium measurements of) neuronal spikes and glial calcium signals (see Figure 4D). Furthermore, given that stimuli/behavior can be structured as occurrence sequences, this approach can directly investigate the interactions between CFUs and stimuli/behavior. For instance, when recording data from a swimming zebrafish, it can aid in identifying swim-related brain regions (see Figure 6D). Finally, the computed dependency can serve as a measure to cluster spatially separated CFUs into CFU groups, potentially unveiling the underlying signaling pathways within the group. For example, when certain brain cells are consistently activated in close temporal proximity, our method can classify these cells together and reveal potential brain circuits through analysis of activation sequences (see Figure S6D).

AQuA2 is implemented as an open-source MATLAB package, a Fiji Plugin, and a cloud-based web service

We provide AQuA2 software across three distinct environments tailored to various demands: a MATLAB-based package; a Fiji[28] plugin written in Java; and a cloud-based online service, AQuA2-Cloud. The MATLAB and Fiji versions allow users to run AQuA2 locally. The MATLAB version makes it easier for users to extend AQuA2, while the Fiji version integrates well into the ImageJ ecosystem. The AQuA2-Cloud enables the offloading of computational tasks to a remote server, which is useful for users without sufficient local computational power for analyzing larger data. This empowers users with lightweight workstations to handle large-scale data through online analysis remotely. All these versions implement the AQuA2 pipeline, offer comprehensive analytical capabilities, provide step-by-step visualization of results, and share a consistent graphical user interface (GUI).

AQuA2's GUI achieves a notable advancement in user-friendliness, compared with its predecessor. We have incorporated intuitive functions for imaging analysis that were previously unavailable in AQuA. For instance, AQuA2's GUI now offers convenient access to capabilities such as image registration, photobleaching correction, and visualization of average curves for manually drawn regions. Additionally, it supports the analysis of 3D data, further enhancing its functionality (see Figure S3). These additions address the preprocessing needs and result examination that were absent in the AQuA GUI. Moreover, we have enhanced the user-controlled parameters to ensure ease of use and alignment with biological principles. Complex parameters and technical intricacies have been abstracted from the GUI, leading to a smoother user experience overall.

AQuA2 improves the accuracy and efficiency of AQuA

To verify the improvements in accuracy, we compare the detection outcomes of AQuA and AQuA2 on three datasets. We first take an *in vivo* calcium recording, which was used in the AQuA paper,[14] as an example (Figure 2A). The results demonstrate that both AQuA2 and AQuA excel in detecting the signal burst of the astrocyte, while AQuA2 identifies the burst as a single, unified entity, which offers a more intuitive representation. We then compare the results on a synthetic dataset with known ground truth (Figure 2B) and a real dataset of astrocyte calcium signals in the spinal cord (Figure 2C). Figures 2B and 2C suggest that AQuA's performance is suboptimal under low SNR or in the presence of large signals. Notably, in the data presented in Figure 2B, we generated a total of 110 real signals. Its low SNR would render signals challenging to detect correctly. However, AQuA detected over 800 events in this scenario, 88% are false positives or negatives, while the error rate for AQuA2 is 7%. Comparisons based on the three datasets suggest that AQuA tends to produce a considerable number of false positives or inaccurately split real signals into trivial fragments while also omitting some significant signals. By contrast, empowered by the top-down framework, AQuA2 demonstrates robust and accurate performance that aligns more closely with human perception even when distinct signals are connected either spatially or temporally.

To demonstrate the efficiency of AQuA2, we compare the execution times across various datasets as illustrated in Table 1. It is worth noting that our comparison focuses solely on the runtime of the event detection pipeline since it occupies over 90% of the overall computation, and the runtime of feature extraction may differ based on the demand of users. As illustrated, AQuA2 is typically around twice as efficient as its predecessor. Notably, when signals in the dataset exhibit more complex patterns, AQuA2 demonstrates greater efficiency up to 40-fold. This improvement in efficiency is attributed to two key factors. First, we have adopted the innovative fast algorithm BILCO for the alignment of propagating signals. Second, the improved accuracy of AQuA2 reduces the number of false positives, thereby decreasing unnecessary computational time.

AQuA2 outperforms peer methods on both synthetic and real datasets

To further substantiate the accuracy of AQuA2, we carried out a comparative assessment of AQuA2's performance against

Table 1. Running time comparison between AQuA2 and AQuA

Data name	Data size (pixels × pixels × frames)	AQuA2	AQuA	AQuA2/AQuA
InVivoSuppRaw (Figure 2A)	481 × 482 × 870	147.94 s	489.64 s	30.2%
Synthetic data (Figure 2B)	512 × 512 × 281	77.80 s	316.68 s	24.6%
Mouse astrocyte calcium (Figure 2C)	422 × 956 × 350	608.84 s	3577.43 s	17.0%
Simulated data (Figure 3A, case 1)	512 × 512 × 250	125.60 s	198.47 s	63.3%
Simulated data (Figure 3A, case 2)	512 × 512 × 250	125.17 s	203.89 s	61.4%
Simulated data (Figure 3A, case 3)	512 × 512 × 250	149.61 s	275.07 s	54.4%
ExVivoSuppRaw (Figure 3B)	502 × 502 × 281	114.23 s	355.14 s	32.2%
Zebrafish myelin sheath (Figure 6B)	2028 × 248 × 300	84.63 s	3200.10 s	2.6%
Mouse *GRAB-ATP* (Figure 6C)	256 × 256 × 3372	105.32 s	206.35 s	51.0%
GlusnfrSuppRaw[14]	199 × 108 × 266	7.32 s	19.98 s	36.6%

AQuA and three other peer tools: suite2p,[12] CaImAn,[11] and Begonia.[16] CaImAn and suite2p are widely used ROI-based methods, while AQuA, Begonia, and AQuA2 are event-based methods. We first evaluated these methods using synthetic data (Figure 3A) under three scenarios frequently observed in real signals: size variability, location variability, and propagation; we then compared their performance on real applications (Figures 3B and 3C). All the methods were fine-tuned to ensure optimal performance. More details about simulation are given in STAR Methods.

Across various scenarios of synthetic data, aside from the specific characteristic we aimed to investigate, the synthetic data were generated without variation in other features. For example, in the scenario with size variability, there is no location variation and signal propagation. Within each scenario, we initially assessed performance under 10 dB SNR and with different degrees of variation—termed "size-change odds," "location-change odds," and "propagation frame," respectively. Then, we evaluated the performance with a moderate variation degree under different SNRs to ensure a comprehensive evaluation. To evaluate the performance, we compared the detection results with known ground truths by using two distinct measures: (1) the F1 score, which represents both precision and recall of detections; and (2) the weighted intersection over union (wIoU), which measures the quality of each detection at the voxel level. The details about the two measures are provided in STAR Methods.

As illustrated in Figure 3A, the three event-based methods, AQuA2, AQuA, and Begonia, consistently demonstrate superior performance on the synthetic data with unfixed size, unfixed location, and propagation, as compared with the ROI-based methods CaImAn and suite2p. This is because ROI-based techniques were initially designed for handling spatially stationary data, making them ill-suited for signals characterized by varying footprints or motion. Among the event-based methods, AQuA2 performs best, consistently achieving F1 scores and wIoU higher than 90% across all experiments and conditions. This highlights that AQuA2 not only exhibits high precision and recall, but it also ensures that each detection closely matches its corresponding ground truth, making it an excellent choice for analyzing non-spatially stationary activities.

In addition to comparing performance on synthetic data, we also evaluated the methods using real data across different scenarios. Figure 3B illustrates their performance on astrocytic calcium imaging data. As expected, owing to inconsistent assumptions about this type of data, ROI-based methods either showed over-segmentation (suite2p) or missed key signals (CaImAn). While Begonia performed adequately on synthetic data, it exhibited over-merging in real data because of its overly simplified assumptions and suboptimal modeling, making it unsuitable for cases with dense signals. By contrast, AQuA and AQuA2 produced consistent results that closely matched the human perception. We also tested neuronal data in Figure 3C, where AQuA2 and ROI-based methods successfully detected the major active cells and yielded similar results. This demonstrates AQuA2's applicability to neuronal data. Importantly, since AQuA2 does not impose size or shape restrictions on CFUs, it can detect small regions that contain repeated signals. These may represent parts of neurons whose main body lies outside the recorded plane. In addition, although some neurons were visible in the background, they were silent during the experiment and were not detected by any method.

AQuA2 identifies signal pattern changes in zebrafish astroglia and neurons under the addition of caffeine

Caffeine, functioning as a central nervous system (CNS) stimulant and an adenosine receptor blocker/antagonist, affects the functions of both neurons and glial cells[29–31] and regulates the brain's internal environment to a certain extent.[29,32] Recent advancements in imaging techniques allow simultaneous observation of glial and neuronal signals, offering an opportunity to explore caffeine's impact on the activity of these cell types. However, owing to the intricate characteristics of glial cell excitation and the distinct dynamics of neuronal and glial signals, there has not been a suitable method for analysis until AQuA2 filled the gap.

Here, we applied AQuA2 to quantify activities and identify functional units of glia and neurons in zebrafish whole brain. The fish expressed green and red calcium sensors in neurons and radial astrocytes, respectively (*Tg(ELAVL3: GCaMP7f; GFAP: jRGECO1B)*). Zebrafish were engaged in fictive swimming in a virtual-reality (VR) environment with (closed loop) and without (open loop) realistic visual feedback during swimming.[33] It underwent two distinct states: normal and drug (where caffeine was added), as shown in Figure 4A. No additional stimulus was introduced.

In Figure 4B, the ΔF and detection results display representative signals in two states. Notably, in the drug state, there are two distinct signal patterns. Pattern 1 mirrors the normal state, exhibiting solely neuronal signals. This pattern may reflect signal activation due to swimming behavior. In contrast, pattern 2 in the drug state reveals astrocytic calcium signals, often accompanied by a larger neuronal signal. This distinct brain activity pattern indicates a change in brain-wide dynamics resulting from the addition of caffeine.

To conduct a comparative analysis between the two states, we utilized AQuA2 to illustrate the CFUs underlying the signal events across different depths, as illustrated in Figure 4C. The CFUs identified within the hindbrain region are believed to be linked to the neuronal circuits involved in zebrafish swimming, as detailed in Chen et al.[34] However, after caffeine addition, a distinct CFU map emerged. While similar CFUs to the normal state were identified, prominent astroglial CFUs and large neuronal CFUs were observed. These findings uncover potential signaling pattern sources activated during brain modulation, which may mediate heightened alertness.

AQuA2 reveals the correlation between neurons and astroglia in zebrafish following the addition of caffeine

Given the pivotal roles glial cells play in supporting, nourishing, and regulating neuronal functions, there has been a growing fascination with the intricate interactions between glial cells and neurons.[35–37] Emerging evidence suggests that glial cells substantially collaborate with neurons in regulating animal behaviors.[33] In the previous section, under the influence of caffeine, there were alterations observed in the signaling patterns of both neurons and astroglial cells. Analyzing the functional units of these two cell types can provide a glimpse into the relationship between these two cell types.

To explore the interactions between astroglial and neuronal signals, we utilized AQuA2 to assess the dependencies between astroglial CFUs and neuronal CFUs in the drug-induced state. In Figure 4D, the most notable correlation pair between astroglial CFU and neuronal CFU is depicted alongside their average curves in two states. The average curve of astroglial CFU remains almost constant in the normal state. However, during caffeine treatment, we observed heightened neuronal activity, increased astroglial activity, and an augmented correlation between neuronal and astroglial signals. This correlation is further highlighted when comparing the extracted spikes with the astroglial ΔF curve, potentially driven by NE after caffeine addition. Caffeine increases arousal and decreases immobility fish swimming in an open-loop environment[38] where swimming leads to NE secretion,[33] which may be responsible for the increase in neuronal and astroglial signals through known astroglial responsivity to NE.[39]

To investigate the activation pattern of the astroglial signal, we employed AQuA2 to visualize the propagation patterns of a single astroglial signal across multiple planes, showcased in Figure 4E. Our analysis revealed an earlier activation of signals in specific brain areas like the caudal and lateral medulla, compared with those in the more medial regions, which experienced a delayed rising time. These findings shed light on the sources of astroglial calcium activity during caffeine exposure, offering potential insights into the pathways facilitating collaboration between astroglia and neurons.

AQuA2 unveils sensorimotor signal propagation patterns in the mouse spinal cord

The spinal cord fulfills critical functions in transmitting sensory information, orchestrating movement, and triggering reflex actions.[40–42] Within the spinal cord, individual laminae contain unique neuronal populations, exhibit distinct connectivity patterns, and serve specialized functional roles.[43,44] A recently introduced miniature one-photon translaminar imaging approach offers the capability for rapid measurements across spinal laminae, providing an opportunity to explore and comprehend the interactions and dynamics inherent to these distinct laminae.[8] Yet, the absence of a mature analysis tool for this novel imaging technique requires researchers to manually partition the FOV into equally sized ROIs for analysis. Given that AQuA2 is an event-based method with versatile applicability, it offers promising and fresh insight into the analysis of such data.

We employed AQuA2 to analyze translaminar astrocyte calcium activity in the spinal dorsal horn of *Tg(GFAP:GCaMP6f)* mice. The experimental setup, depicted in Figure 5A, involved securing the mouse on a spherical treadmill and optically recording GCaMP6f activity through a microprism implanted near the lateral edge of the spinal gray matter.[8] During the recordings, a pressure stimulus was applied to the mouse's proximal tail. The mouse's motor behavior was tracked concomitantly (STAR Methods). As illustrated in Figures 5A–5C, the pinch elicited noticeable calcium activity within the dorsal regions of the FOV, revealing this spinal region's response to the sensory stimulus. Within the same recording, AQuA2 also detected two motor behavior-evoked calcium signals that were missed by the ROI analysis mentioned above.

To determine the distinguishing features between these sensory- and motor-evoked signals, we utilized AQuA2 to visualize their respective signal propagation patterns. As depicted in Figure 5C, the sensory-evoked signal displayed a propagation pattern starting from the dorsal side, while the motor-evoked signals emanated from the ventral side. The findings suggest that peripheral sensory stimuli and motor actions engage neural circuits in distinct spinal laminae, that astrocytes' activity patterns reflect this neural activity, and that the astrocyte excitation can propagate across spinal laminae on a seconds timescale in behaving mice. This discovery has implications for how astrocytes might regulate spinal neural circuit activity or plasticity and underscores AQuA2's ability to uncover new biological phenomena leading to testable hypotheses about cell or circuit function.

Additionally, beyond the translaminar signals, Figure 5D illustrates the detection of local signals within spinal laminae of the same mouse during a different trial. These signals, often missed by other methods, imply the existence of localized functional units, akin to those observed in the brain.

AQuA2 quantifies signals across biosensors, cell types, organs, animal models, microscopy techniques, and imaging approaches

The recent advancements in indicators and imaging techniques have facilitated the recording of diverse molecular

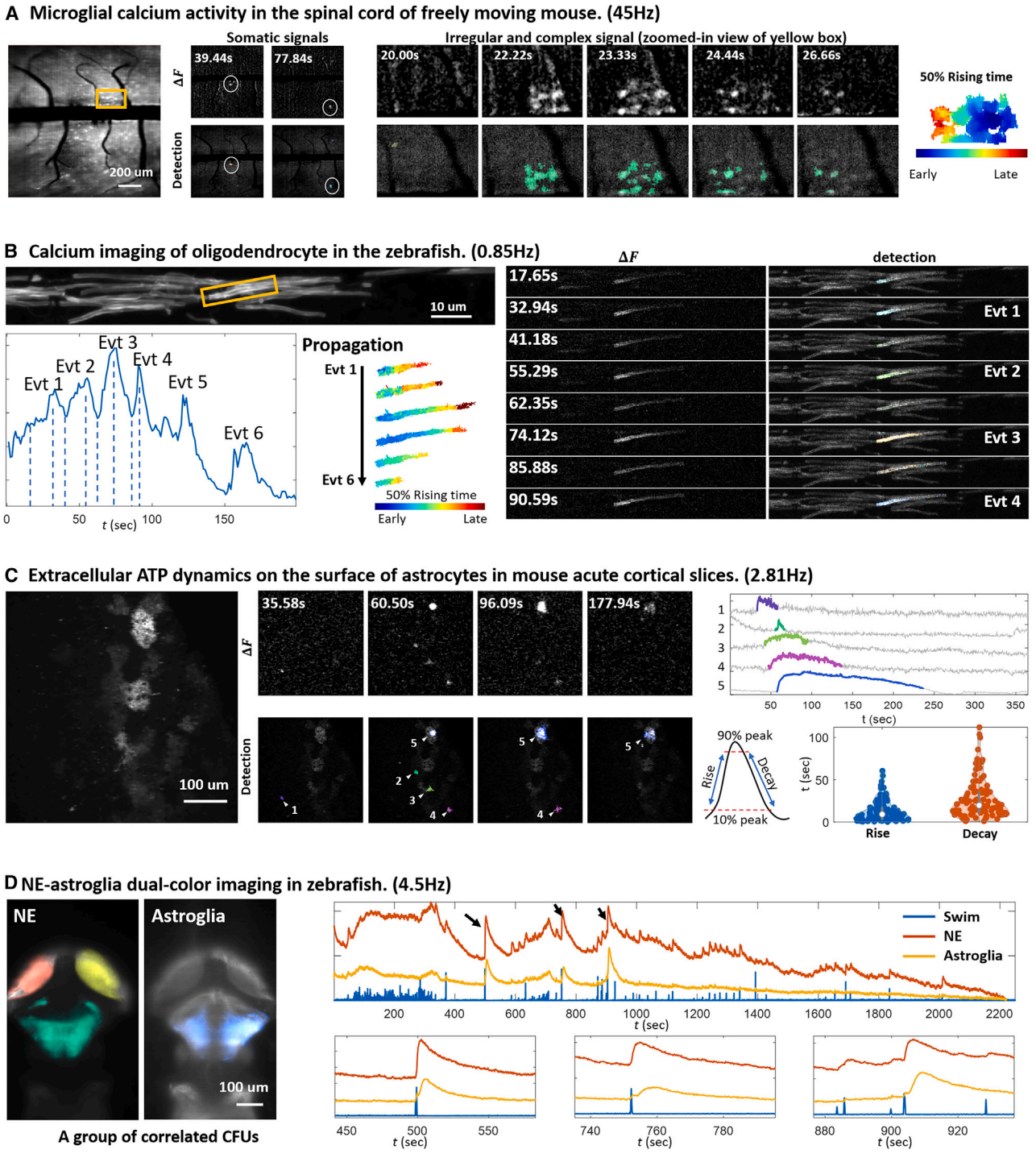

Figure 6. AQuA2 quantifies signals across biosensors, cell types, organs, animal models, and microscopy techniques

(A) Application of AQuA2 to quantifying the signals from mouse spinal microglia (expressed by *Tg(CX3CR1:GCaMP5g)*) imaging data. The comparison between Δ*F* and detection for both circular signals and the spatially complex signal (shown in a zoomed-in view of the selected orange box) is provided. On the right, the quantified propagation pattern of the spatially complex signal is given, with blue denoting early rising time and red denoting late rising time.

(B) Application of AQuA2 for accurate quantification of distinct oligodendrocyte calcium dynamics within the CNS myelin sheath of zebrafish. The calcium was expressed through *Tg(mbp:memGCaMP7s)*. The average curve of the region of interest (labeled by yellow) is depicted in the bottom-left. In the bottom-middle, the propagation pattern of events is showcased, with earlier activation represented in blue and later rising times in red. On the right, a comparison between Δ*F* and AQuA2 results is provided, with each colored region representing a distinct detection.

(legend continued on next page)

spatiotemporal activities, including ATP,[6] glutamate,[45] γ-aminobutyric acid (GABA),[46] serotonin,[47] NE,[5] and others, significantly aiding research into mechanism studies for both physiological and abnormal states at the cellular and subcellular levels. Despite this progress, signals of numerous molecular sensors lack dedicated analysis methods. AQuA2 will serve as a broadly applicable tool for filling this gap.

To validate the ability of AQuA2 to quantify and analyze signals of various types, we conducted tests on datasets encompassing a variety of animals, cell types, molecular sensors, organs, microscopy techniques, and imaging approaches. Owing to space constraints, only four applications are depicted in Figure 6, with more in Figures S5–S7. All the tested scenarios are clearly listed in Table S1 with the associated parameter settings downloadable.

AQuA2 can detect microglial calcium activity in the spinal cord of a mouse, as shown in Figure 6A. These transients were recorded in the superficial dorsal horn of behaving *Tg(CX3CR1: GCaMP5g-tdTomato)* mice, using a wearable macroscope.[48] Both somatic signals and signals with irregular shapes and complex spatiotemporal features were identified. AQuA2, therefore, can detect signals with distinct spatiotemporal characteristics in the same dataset, including localized and propagating cellular activity.

AQuA2 was also employed to detect and visualize temporally dense oligodendrocyte calcium activities within CNS myelin sheaths, as illustrated in Figure 6B. The calcium sensor was expressed around the membrane using the zebrafish line *Tg(mbp:memGCaMP7s)*. The calcium transients distinctly exhibit signal propagation along the myelin sheath and form interconnected patterns in the temporal dimension. The propagation and interconnectedness pose a challenge for other analysis tools. However, by leveraging AQuA2, each transient was effectively isolated and quantified, accompanied by a clear visualization of its propagation pattern. This successful application underscores the capability of AQuA2 to handle intricate and complex signals.

We also tested how AQuA2 detects biological signals other than calcium. Using AQuA2, we quantified extracellular ATP dynamics captured by the *GRAB-ATP*[6] sensor on the surface of astrocytes in acute cortical slices. As depicted in Figure 6C, ATP signals exhibit heterogeneous temporal characteristics, ranging from long-lasting (hundreds of seconds) to relatively brief (less than ten seconds). Despite this heterogeneity, AQuA2 successfully detects them using the same parameter setting, showcasing its ability to detect signals with diverse spatial and temporal characteristics.

The relationship between NE signals and astroglial calcium signals within the brain is also an area of investigation for biological researchers. Employing AQuA2 on a dual-color dataset in zebrafish, which captures NE and astroglial calcium signals in separate channels (*Tg(ELAVL3: GRABNE; GFAP: jRGECO)*) and records zebrafish swim commands via electrophysiology, we identified and visualized swim-related CFUs, as depicted in Figure 6D. Upon analyzing the curves across different channels, the results demonstrate a notable occurrence: following zebrafish swim spikes, NE and astroglial signals manifested in pairs. This observation is consistent with behavior-generating circuits engaging both NE signaling and astroglial calcium activity.

In addition to the applications mentioned above, cases for its further use are shown in Figures S5 and S6, encompassing zebrafish Ach signals, zebrafish dopamine signals, and zebrafish dual-color data featuring ATP and neuronal calcium signals, among others. The application to dendritic signals is shown with dynamic and overlapping spatial footprints clearly observable in Figure S6E, further supporting the usefulness of AQuA2 for non-somatic neuronal signals. As multi-session imaging across multiple days becomes more and more prevalent, we demonstrated AQuA2's applicability in this scenario, as in Figure S7, where common and session-specific CFUs can be identified. Collectively, AQuA2 can be effectively utilized to quantify and analyze signals across a variety of molecular sensors, cell types, organs, animal models, microscopy techniques, and imaging approaches, consistently providing highly informative results.

DISCUSSION

While advanced genetic fluorescent probes and imaging techniques have unleashed the potential for neurotransmitter, neuromodulator, and other molecular-level studies, the corresponding analysis tools have not progressed at the same pace. This situation necessitates researchers devising their own analysis pipelines or attempting to adapt mismatched analysis tools. In response to this need, we developed AQuA2, an improved version of AQuA, with greater accuracy, efficiency, versatility, and many innovative functions.

Compared with existing approaches, AQuA2 can quantify and analyze a more diverse range of signals and low SNR scenarios, a capability that AQuA lacks. For instance, as illustrated in Figures 2B and C, the limitations of AQuA's framework become evident when the target signal with large noise occupies a large spatial area, leading to the frequent misidentification of broad signals as multiple unclear small events—an issue mentioned by Rupprecht et al.[49] Additionally, AQuA also struggles to effectively detect signals with longer durations, while AQuA2 successfully identifies signals >100s (Figure 6C). AQuA may erroneously identify any short temporal fluctuations as events, even when the duration of the longer target signal is presumed, particularly in low SNR scenarios

(C) Application of AQuA2 for the quantification of extracellular ATP dynamics, captured by the *GRAB-ATP* sensor[6] and two-photon microscope, on the surface of astrocytes in acute cortical slices. Example representative events (marked by white triangles) are presented with their corresponding average curves (event duration is indicated by the event color). Statistical analysis of event temporal features (rising duration and decay duration) is provided on the bottom-right.
(D) Application of AQuA2 for identifying the swim-related regions on a light-sheet norepinephrine (NE)-astroglia dual-color recording of zebrafish. NE was expressed by *Tg(ELAVL3: GRABNE)*, and astroglial calcium was expressed by *Tg(GFAP: jRGECO)*. On the left, each colored region represents a swim-related CFU. On the right, swim strength (blue) and average curves of two channels (red and yellow) are depicted. Three zoomed-in figures are provided for three signals. More applications and testing can be found in Figures S5, S6, and S7. See STAR Methods for experimental details.

(Figure 2C). AQuA2 addresses these issues by embracing a different framework, incorporating prior knowledge in the early stage, and making a set of technical innovations. As a result, AQuA2 can perform flexible detection across diverse biosensors, cell types, organs, animal models, microscopy techniques, and imaging approaches, verified by our real applications, as shown in Figures 6, S6, and S7.

The development of the CFU analysis effectively bridges the gap between ROI-based and event-based methods. It serves as a more flexible version of ROI, tolerating the variation between signals activated from the same source. This flexibility is crucial, because in many datasets, the territories of signals emanating from the same source are often not fixed. That will violate the assumption of ROI-based methods, while event-based methods lack the ability to analyze the region behind events. The CFU module fills this gap, enabling the analysis of functional units behind events with variation. To probe the functional relationship between CFUs, a statistical approach was developed, taking event occurrence sequences as input. This allows AQuA2 to reveal interrelationships between functional units with different waveforms, such as neuronal CFU with spike signals and astroglial CFU with bell-shaped signals (Figure 4D). Interactions between CFU and stimulus/behavior can also be analyzed (Figure 6D), and the estimated dependency could serve as a distance measure to group CFUs into potential circuits (Figure S6D).

Propagation analysis, a key feature of AQuA, is seamlessly integrated and optimized in AQuA2. It employs joint alignment techniques to match all time points among pixel curves and the reference curve. In contrast to the correlation-based approach, which relies on matching the entire curve and is consequently vulnerable to waveform variations, leading to suboptimal results, joint alignment analysis offers greater flexibility and the ability to provide rich, precise information, as shown in Figure S1E. However, the long computation time and large memory usage have been obstacles in using AQuA for many users. This challenge is particularly pronounced when dealing with spatially large events, where an increased number of pixels escalates the problem's scale. For instance, in the past, propagation analysis like Figure 5C would lead to memory overflow on our workstation as the event occupies the whole FOV. The adoption of our previously proposed algorithm, BILCO,[24] has solved this problem. Compared with the propagation analysis in AQuA, it now completes the analysis in only 1/10th of the time and with 1/10th of memory usage, enabling AQuA2 to efficiently examine the propagation patterns of spatially large signals.

In addition to the improvements discussed above, AQuA2 enhances accessibility and usability. Three versions of the same pipeline were implemented for different users, each offering unique advantages. For instance, the MATLAB version allows direct code modification and debugging, enabling researchers to adjust the analysis for their data. The Fiji plugin version supports integration with other Fiji plugins and usage across different systems (Windows, Linux, and Mac) without requiring environment installation. AQuA2-Cloud offers online analysis, offloading computations to a remote server. Furthermore, AQuA2 adopts clear and user-friendly parameters, eliminating previously confusing settings in AQuA and ensuring ease of use without significant usability barriers.

We have demonstrated quite a few applications of AQuA2 across various challenges, encompassing the quantification of diverse signals, visualization of signal propagation patterns, analysis of 3D time-lapse imaging data, integration of multi-session imaging experiments, and investigation of interactions among different signal types in dual-color data. All the tested scenarios have been clearly listed in Table S1, highlighting the key experiment configuration. The optimized parameter settings for all test scenarios are also provided so that they can be adopted for similar applications.

As data-driven and machine-learning principles were used to guide our design of AQuA2, we envision a broad spectrum of potential applications beyond what we have tested so far. First, AQuA2 can be potentially extended to the organs and cell types beyond the CNS. Complex spatiotemporal molecular signals are observed in almost every body part besides CNS. For instance, Ach is released in the pancreas to regulate insulin secretion,[26] and the calcium signaling in the liver[50] modulates various functions such as bile secretion, glucose metabolism, cell proliferation, and apoptosis. Second, AQuA2 can be potentially applied with many recently developed molecular sensors, such as GABA,[46] serotonin,[47] protein kinase A (PKA),[51] and cAMP, to name but a few.[52] Analysis demands for these new signals are expected to increase as the sensors get better at revealing more complex and richer spatiotemporal patterns, just like what calcium sensors have gone through. Third, AQuA2 can be potentially compatible with negative signals. With simple linear transforms such as a negative transform plus a shift to assure non-negativity, the negative signals will become positive. However, users should exercise caution when considering such application scenarios and should conduct thorough validation and examination. They are encouraged to reach out for assistance with this validation and refinement, as the AQuA2 development team is committed to supporting the research community.

Limitations of the study

With easy access and the anticipated widespread usage, it is important to know the limitations of AQuA2 to avoid misuse or misinterpretation. First, similar to all automated detection methods that we tested, AQuA2 neglects silent cells or functional regions, even if they are visible in the background (e.g., Figure 3C), as its detection mechanism relies on dynamic fluorescence changes. When calculating the proportion of task-related or region-specific cells, silent cells should be identified using alternative algorithms. The identification of silent functional regions also has the potential to enhance the CFU analysis, since it may inform a new way to group related CFUs belonging to the same cell or structure. Future efforts are needed to address this important issue. Second, for stereotypical neuronal nuclear or somatic calcium signals, AQuA2's performance may not exceed that of ROI-based methods, as ROI assumptions align well with neuronal dynamics. But for neuropil analysis, AQuA2 may perform better, as the assumptions of ROI-based methods may not hold, given the possible compartmental signals and the near-impossibility of achieving perfect stabilization at the axon/dendrite-scale tissue level (Figure S6E). Third, AQuA2 pipeline includes rigid motion correction in the preprocessing step; however, data collected from live animals may involve

non-rigid motion, which can result in false positives during detection. For such data, users may need to apply additional preprocessing tailored to the specific motion characteristics before using AQuA2 for analysis.

RESOURCE AVAILABILITY

Lead contact

Further information and requests for resources and reagents should be directed to and will be fulfilled by the lead contact, Guoqiang Yu (yug@tsinghua.edu.cn).

Materials availability

Zebrafish lines generated in this study will be available upon request from Misha Ahrens (ahrensm@janelia.hhmi.org) or David Lyons (david.lyons@ed.ac.uk).

Data and code availability

- The raw data reported in this paper are either shared through Mendeley with the dataset identifier https://dx.doi.org/10.17632/9f5myhx6jy or will be shared by the lead contact upon request due to the size limit of Mendeley.
- The raw data related to Figure 2A are available at https://drive.google.com/file/d/1TjfFzlg_6BxsFX_l3-P92M5Rp_5j6wiM/view.
- The raw data related to Figure 3B are available at https://drive.google.com/file/d/13tNSFQ1BFV__42TY0lZbHd1VYTRfNyfD/view.
- The raw data related to Figure S6E are available at https://dandiarchive.org/dandiset/000037/0.240209.1623.
- The raw data related to Figure S7 are available at https://users.flatironinstitute.org/~neuro/caiman_paper/K53.html.
- All original code has been deposited at https://github.com/yu-lab-vt/AQuA2.
- Any additional information required to reanalyze the data reported in this paper is available from the lead contact upon request.

ACKNOWLEDGMENTS

This work was primarily supported by the National Institutes of Health (NIH) grant U19NS123719 (to G.Y. and A.N.). It was partially supported by NIH grants R01MH110504 (to G.Y.), R01NS099254 (to K.E.P.), R01MH121446 (to K.E.P.), U19NS112959 (to A.N.), and NSF CAREER 1942360 (to K.E.P.); the Howard Hughes Medical Institute (to M.B.A.); the Sol Goldman Charitable Trust (to A.N.); equipment funds from C. and L. Greenfield (to A.N.); STI2030-Major Projects (2021ZD0202300 to S.-H.S.), National Natural Science Foundation of China (32021002 to S.-H.S.), New Cornerstone Investigator Program (to S.-H.S.); the Edwards-Yeckel Research Foundation (to A.N.), a Wellcome Trust Senior Research Fellowship (214244/Z/18/Z to D.A.L.); Marie Skłodowska-Curie action "Zenith" (H2020-MSCA-ITN-2018 813457 to D.A.L.); and an Elite network of Bavaria/ENB Biological physics program award (to P.N.B.). The content is solely the authors' responsibility and does not necessarily represent the official views of the NIH or other funding agencies.

AUTHOR CONTRIBUTIONS

Conceptualization, G.Y.; methodology, X.M. and G.Y.; software, X.M. and M.B.; investigation, A.B.-Y.C., D.D., E.C., C.R.T., P.N.B., R.G.A., J.-X.L., V.M.S.R., W. Zhang, M.E.R., Y.H., X.W., L.L., H.F.D., S.-H.S., K.E.P., D.A.L., A.N., and M.B.A.; writing – original draft, X.M. and G.Y.; writing – review and editing, X.M., M.B., Y.W., M.W., W. Zhang, W. Zheng, K.E.P., D.A.L., A.N., M.B.A., and G.Y.; supervision, H.F.D., S.-H.S., K.E.P., D.A.L., A.N., M.B.A., and G.Y.

DECLARATION OF INTERESTS

The authors declare no competing interests.

STAR★METHODS

Detailed methods are provided in the online version of this paper and include the following:

- KEY RESOURCES TABLE
- EXPERIMENTAL MODEL AND STUDY PARTICIPANT DETAILS
  - Animals
  - Transgenesis
- METHOD DETAILS
  - Data collection
  - Synthetic data generation
  - AQuA2 event detection pipeline
  - AQuA2 CFU identification
  - Application scenarios and corresponding AQuA2 parameter settings
- QUANTIFICATION AND STATISTICAL ANALYSIS
  - Workstation configuration
  - Event evaluation for ROI-based methods

SUPPLEMENTAL INFORMATION

Supplemental information can be found online at https://doi.org/10.1016/j.cell.2025.03.012.

Received: May 31, 2024
Revised: January 13, 2025
Accepted: March 6, 2025
Published: April 8, 2025

REFERENCES

1. Bear, M., Connors, B., and Paradiso, M.A. (2020). Neuroscience: Exploring the brain, enhanced edition: Exploring the brain (Jones & Bartlett Learning).
2. Kelly, R.B. (1993). Storage and release of neurotransmitters. Cell *72*, 43–53. https://doi.org/10.1016/s0092-8674(05)80027-3.
3. Meldrum, B.S. (2000). Glutamate as a neurotransmitter in the brain: review of physiology and pathology. J. Nutr. *130*, 1007S–1015S. https://doi.org/10.1093/jn/130.4.1007S.
4. Miyazaki, S., Shirakawa, H., Nakada, K., and Honda, Y. (1993). Essential role of the inositol 1, 4, 5-trisphosphate receptor/Ca2+ release channel in Ca2+ waves and Ca2+ oscillations at fertilization of mammalian eggs. Developmental biology *158*, 62–78.
5. Feng, J., Zhang, C., Lischinsky, J.E., Jing, M., Zhou, J., Wang, H., Zhang, Y., Dong, A., Wu, Z., Wu, H., et al. (2019). A genetically encoded fluorescent sensor for rapid and specific in vivo detection of norepinephrine. Neuron *102*, 745–761.e8. https://doi.org/10.1016/j.neuron.2019.02.037.
6. Wu, Z., He, K., Chen, Y., Li, H., Pan, S., Li, B., Liu, T., Xi, F., Deng, F., Wang, H., et al. (2022). A sensitive GRAB sensor for detecting extracellular ATP in vitro and in vivo. Neuron *110*, 770–782.e5. https://doi.org/10.1016/j.neuron.2021.11.027.
7. Masharina, A., Reymond, L., Maurel, D., Umezawa, K., and Johnsson, K. (2012). A fluorescent sensor for GABA and synthetic $GABA_B$ receptor ligands. J. Am. Chem. Soc. *134*, 19026–19034. https://doi.org/10.1021/ja306320s.
8. Shekhtmeyster, P., Carey, E.M., Duarte, D., Ngo, A., Gao, G., Nelson, N.A., Clark, C.L., and Nimmerjahn, A. (2023). Multiplex translaminar imaging in the spinal cord of behaving mice. Nat. Commun. *14*, 1427. https://doi.org/10.1038/s41467-023-36959-2.
9. Herman, B. (2020). Fluorescence microscopy (Garland Science) https://doi.org/10.1201/9781003077060.
10. Aswendt, M., Schwarz, M., Abdelmoula, W.M., Dijkstra, J., and Dedeurwaerdere, S. (2017). Whole-brain microscopy meets in vivo neuroimaging: techniques, benefits, and limitations. Mol. Imaging Biol. *19*, 1–9. https://doi.org/10.1007/s11307-016-0988-z.

11. Giovannucci, A., Friedrich, J., Gunn, P., Kalfon, J., Brown, B.L., Koay, S.A., Taxidis, J., Najafi, F., Gauthier, J.L., Zhou, P., et al. (2019). CaImAn an open source tool for scalable calcium imaging data analysis. eLife *8*, e38173. https://doi.org/10.7554/eLife.38173.

12. Pachitariu, M., Stringer, C., Dipoppa, M., Schröder, S., Rossi, L.F., Dalgleish, H., Carandini, M., and Harris, K.D. (2017). Suite2p: beyond 10,000 neurons with standard two-photon microscopy. Preprint at bioRxiv, 061507.

13. Agarwal, A., Wu, P.-H., Hughes, E.G., Fukaya, M., Tischfield, M.A., Langseth, A.J., Wirtz, D., and Bergles, D.E. (2017). Transient opening of the mitochondrial permeability transition pore induces microdomain calcium transients in astrocyte processes. Neuron *93*, 587–605.e7. https://doi.org/10.1016/j.neuron.2016.12.034.

14. Wang, Y., DelRosso, N.V., Vaidyanathan, T.V., Cahill, M.K., Reitman, M.E., Pittolo, S., Mi, X., Yu, G., and Poskanzer, K.E. (2019). Accurate quantification of astrocyte and neurotransmitter fluorescence dynamics for single-cell and population-level physiology. Nat. Neurosci. *22*, 1936–1944. https://doi.org/10.1038/s41593-019-0492-2.

15. Kustikova, V., Krivonosov, M., Pimashkin, A., Denisov, P., Zaikin, A., Ivanchenko, M., Meyerov, I., and Semyanov, A. (2018). CalciumCV: Computer vision software for calcium signaling in astrocytes. In International Conference on Analysis of Images, Social Networks and Texts (Springer), pp. 168–179.

16. Bjørnstad, D.M., Åbjørsbråten, K.S., Hennestad, E., Cunen, C., Hermansen, G.H., Bojarskaite, L., Pettersen, K.H., Vervaeke, K., and Enger, R. (2021). Begonia—a two-photon imaging analysis pipeline for astrocytic ca2+ signals. Front. Cell. Neurosci. *15*, 681066. https://doi.org/10.3389/fncel.2021.681066.

17. Zhou, P., Resendez, S.L., Rodriguez-Romaguera, J., Jimenez, J.C., Neufeld, S.Q., Giovannucci, A., Friedrich, J., Pnevmatikakis, E.A., Stuber, G.D., Hen, R., et al. (2018). Efficient and accurate extraction of in vivo calcium signals from microendoscopic video data. eLife *7*, e28728. https://doi.org/10.7554/eLife.28728.

18. Hughes, A.N., and Appel, B. (2020). Microglia phagocytose myelin sheaths to modify developmental myelination. Nat. Neurosci. *23*, 1055–1066. https://doi.org/10.1038/s41593-020-0654-2.

19. de Ceglia, R., Ledonne, A., Litvin, D.G., Lind, B.L., Carriero, G., Latagliata, E.C., Bindocci, E., Di Castro, M.A., Savtchouk, I., Vitali, I., et al. (2023). Specialized astrocytes mediate glutamatergic gliotransmission in the CNS. Nature *622*, 120–129. https://doi.org/10.1038/s41586-023-06502-w.

20. Reitman, M.E., Tse, V., Mi, X., Willoughby, D.D., Peinado, A., Aivazidis, A., Myagmar, B.-E., Simpson, P.C., Bayraktar, O.A., Yu, G., et al. (2023). Norepinephrine links astrocytic activity to regulation of cortical state. Nat. Neurosci. *26*, 579–593. https://doi.org/10.1038/s41593-023-01284-w.

21. Venkataramani, V., Yang, Y., Schubert, M.C., Reyhan, E., Tetzlaff, S.K., Wißmann, N., Botz, M., Soyka, S.J., Beretta, C.A., Pramatarov, R.L., et al. (2022). Glioblastoma hijacks neuronal mechanisms for brain invasion. Cell *185*, 2899–2917.e31. https://doi.org/10.1016/j.cell.2022.06.054.

22. Guo, S.-M., Veneziano, R., Gordonov, S., Li, L., Danielson, E., Perez de Arce, K., Park, D., Kulesa, A.B., Wamhoff, E.-C., Blainey, P.C., et al. (2019). Multiplexed and high-throughput neuronal fluorescence imaging with diffusible probes. Nat. Commun. *10*, 4377. https://doi.org/10.1038/s41467-019-12372-6.

23. Kelner, A., Leitão, N., Chabaud, M., Charpentier, M., and de Carvalho-Niebel, F. (2018). Dual color sensors for simultaneous analysis of calcium signal dynamics in the nuclear and cytoplasmic compartments of plant cells. Front. Plant Sci. *9*, 245. https://doi.org/10.3389/fpls.2018.00245.

24. Mi, X., Wang, M., Chen, A., Lim, J.-X., Wang, Y., Ahrens, M.B., and Yu, G. (2022). BILCO: An Efficient Algorithm for Joint Alignment of Time Series. Adv. Neural Inf. Process. Syst. *35*, 36270–36281.

25. Patriarchi, T., Cho, J.R., Merten, K., Howe, M.W., Marley, A., Xiong, W.-H., Folk, R.W., Broussard, G.J., Liang, R., Jang, M.J., et al. (2018). Ultrafast neuronal imaging of dopamine dynamics with designed genetically encoded sensors. Science *360*, eaat4422. https://doi.org/10.1126/science.aat4422.

26. Jing, M., Zhang, P., Wang, G., Feng, J., Mesik, L., Zeng, J., Jiang, H., Wang, S., Looby, J.C., Guagliardo, N.A., et al. (2018). A genetically encoded fluorescent acetylcholine indicator for in vitro and in vivo studies. Nat. Biotechnol. *36*, 726–737. https://doi.org/10.1038/nbt.4184.

27. Lee, D., and Seung, H.S. (2000). Algorithms for non-negative matrix factorization. Adv. Neural Inf. Process. Syst. *13*.

28. Schindelin, J., Arganda-Carreras, I., Frise, E., Kaynig, V., Longair, M., Pietzsch, T., Preibisch, S., Rueden, C., Saalfeld, S., Schmid, B., et al. (2012). Fiji: an open-source platform for biological-image analysis. Nat. Methods *9*, 676–682. https://doi.org/10.1038/nmeth.2019.

29. Nehlig, A., Daval, J.L., and Debry, G. (1992). Caffeine and the central nervous system: mechanisms of action, biochemical, metabolic and psychostimulant effects. Brain Res. Brain Res. Rev. *17*, 139–170. https://doi.org/10.1016/0165-0173(92)90012-b.

30. Khairnar, A., Plumitallo, A., Frau, L., Schintu, N., and Morelli, M. (2010). Caffeine enhances astroglia and microglia reactivity induced by 3,4-methylenedioxymethamphetamine ('ecstasy') in mouse brain. Neurotox. Res. *17*, 435–439. https://doi.org/10.1007/s12640-009-9125-y.

31. Othman, M.A., Fadel, R., Tayem, Y., Jaradat, A., Rashid, A., Fatima, A., Al-Mahameed, A.E., and Nasr El-Din, W.A. (2023). Caffeine protects against hippocampal alterations in type 2 diabetic rats via modulation of gliosis, inflammation and apoptosis. Cell Tissue Res. *392*, 443–466. https://doi.org/10.1007/s00441-022-03735-5.

32. Fredholm, B.B. (1995). Adenosine, adenosine receptors and the actions of caffeine. Pharmacol. Toxicol. *76*, 93–101. https://doi.org/10.1111/j.1600-0773.1995.tb00111.x.

33. Mu, Y., Bennett, D.V., Rubinov, M., Narayan, S., Yang, C.-T., Tanimoto, M., Mensh, B.D., Looger, L.L., and Ahrens, M.B. (2019). Glia accumulate evidence that actions are futile and suppress unsuccessful behavior. Cell *178*, 27–43.e19. https://doi.org/10.1016/j.cell.2019.05.050.

34. Chen, A.B., Duque, M., Wang, V.M., Dhanasekar, M., Mi, X., Rymbek, A., Tocquer, L., Narayan, S., Prober, D., Yu, G., et al. (2024). Norepinephrine changes behavioral state via astroglial purinergic signaling. Preprint at bioRxiv. https://doi.org/10.1101/2024.05.23.595576.

35. Araque, A. (2006). Astrocyte-neuron signaling in the brain–implications for disease. Curr. Opin. Investig. Drugs *7*, 619–624.

36. Halassa, M.M., Fellin, T., and Haydon, P.G. (2007). The tripartite synapse: roles for gliotransmission in health and disease. Trends Mol. Med. *13*, 54–63. https://doi.org/10.1016/j.molmed.2006.12.005.

37. Um, J.W. (2017). Roles of glial cells in sculpting inhibitory synapses and neural circuits. Front. Mol. Neurosci. *10*, 381. https://doi.org/10.3389/fnmol.2017.00381.

38. Chen, X., Mu, Y., Hu, Y., Kuan, A.T., Nikitchenko, M., Randlett, O., Chen, A.B., Gavornik, J.P., Sompolinsky, H., Engert, F., et al. (2018). Brain-wide organization of neuronal activity and convergent sensorimotor transformations in larval zebrafish. Neuron *100*, 876–890.e5. https://doi.org/10.1016/j.neuron.2018.09.042.

39. Paukert, M., Agarwal, A., Cha, J., Doze, V.A., Kang, J.U., and Bergles, D.E. (2014). Norepinephrine controls astroglial responsiveness to local circuit activity. Neuron *82*, 1263–1270. https://doi.org/10.1016/j.neuron.2014.04.038.

40. Courtine, G., Gerasimenko, Y., Van Den Brand, R., Yew, A., Musienko, P., Zhong, H., Song, B., Ao, Y., Ichiyama, R.M., Lavrov, I., et al. (2009). Transformation of nonfunctional spinal circuits into functional states after the loss of brain input. Nat. Neurosci. *12*, 1333–1342. https://doi.org/10.1038/nn.2401.

41. Heimer, L. (2012). The Human Brain and Spinal Cord: Functional Neuroanatomy and Dissection Guide (Springer Science & Business Media).

42. Filli, L., Engmann, A.K., Zörner, B., Weinmann, O., Moraitis, T., Gullo, M., Kasper, H., Schneider, R., and Schwab, M.E. (2014). Bridging the gap: a reticulo-propriospinal detour bypassing an incomplete spinal cord injury. J. Neurosci. *34*, 13399–13410. https://doi.org/10.1523/JNEUROSCI.0701-14.2014.

43. Todd, A.J. (2010). Neuronal circuitry for pain processing in the dorsal horn. Nat. Rev. Neurosci. *11*, 823–836. https://doi.org/10.1038/nrn2947.

44. Abraira, V.E., and Ginty, D.D. (2013). The sensory neurons of touch. Neuron *79*, 618–639. https://doi.org/10.1016/j.neuron.2013.07.051.

45. Marvin, J.S., Borghuis, B.G., Tian, L., Cichon, J., Harnett, M.T., Akerboom, J., Gordus, A., Renninger, S.L., Chen, T.-W., Bargmann, C.I., et al. (2013). An optimized fluorescent probe for visualizing glutamate neurotransmission. Nat. Methods *10*, 162–170. https://doi.org/10.1038/nmeth.2333.

46. Marvin, J.S., Shimoda, Y., Magloire, V., Leite, M., Kawashima, T., Jensen, T.P., Kolb, I., Knott, E.L., Novak, O., Podgorski, K., et al. (2019). A genetically encoded fluorescent sensor for in vivo imaging of GABA. Nat. Methods *16*, 763–770. https://doi.org/10.1038/s41592-019-0471-2.

47. Wan, J., Peng, W., Li, X., Qian, T., Song, K., Zeng, J., Deng, F., Hao, S., Feng, J., Zhang, P., et al. (2021). A genetically encoded sensor for measuring serotonin dynamics. Nat. Neurosci. *24*, 746–752. https://doi.org/10.1038/s41593-021-00823-7.

48. Shekhtmeyster, P., Duarte, D., Carey, E.M., Ngo, A., Gao, G., Olmstead, J.A., Nelson, N.A., and Nimmerjahn, A. (2023). Trans-segmental imaging in the spinal cord of behaving mice. Nat. Biotechnol. *41*, 1729–1733. https://doi.org/10.1038/s41587-023-01700-3.

49. Rupprecht, P., Duss, S.N., Becker, D., Lewis, C.M., Bohacek, J., and Helmchen, F. (2024). Centripetal integration of past events in hippocampal astrocytes regulated by locus coeruleus. Nat. Neurosci. *27*, 927–939. https://doi.org/10.1038/s41593-024-01612-8.

50. Amaya, M.J., and Nathanson, M.H. (2013). Calcium signaling in the liver. Compr. Physiol. *3*, 515–539. https://doi.org/10.1002/cphy.c120013.

51. Zhang, J.-F., Liu, B., Hong, I., Mo, A., Roth, R.H., Tenner, B., Lin, W., Zhang, J.Z., Molina, R.S., Drobizhev, M., et al. (2021). An ultrasensitive biosensor for high-resolution kinase activity imaging in awake mice. Nat. Chem. Biol. *17*, 39–46. https://doi.org/10.1038/s41589-020-00660-y.

52. Massengill, C.I., Bayless-Edwards, L., Ceballos, C.C., Cebul, E.R., Cahill, J., Bharadwaj, A., Wilson, E., Qin, M., Whorton, M.R., Baconguis, I., et al. (2022). Sensitive genetically encoded sensors for population and subcellular imaging of cAMP in vivo. Nat. Methods *19*, 1461–1471. https://doi.org/10.1038/s41592-022-01646-5.

53. Gillon, C.J., Lecoq, J.A., Pina, J.E., Ahmed, R., Billeh, Y.N., Caldejon, S., Groblewski, P., Henley, T.M., Kato, I., Lee, E., et al. (2023). Responses of pyramidal cell somata and apical dendrites in mouse visual cortex over multiple days. Sci. Data *10*, 287. https://doi.org/10.1038/s41597-023-02214-y.

54. Garcia, A.D.R., Doan, N.B., Imura, T., Bush, T.G., and Sofroniew, M.V. (2004). GFAP-expressing progenitors are the principal source of constitutive neurogenesis in adult mouse forebrain. Nat. Neurosci. *7*, 1233–1241. https://doi.org/10.1038/nn1340.

55. Madisen, L., Garner, A.R., Shimaoka, D., Chuong, A.S., Klapoetke, N.C., Li, L., Van Der Bourg, A., Niino, Y., Egolf, L., Monetti, C., et al. (2015). Transgenic mice for intersectional targeting of neural sensors and effectors with high specificity and performance. Neuron *85*, 942–958. https://doi.org/10.1016/j.neuron.2015.02.022.

56. Yona, S., Kim, K.-W., Wolf, Y., Mildner, A., Varol, D., Breker, M., Strauss-Ayali, D., Viukov, S., Guilliams, M., Misharin, A., et al. (2013). Fate mapping reveals origins and dynamics of monocytes and tissue macrophages under homeostasis. Immunity *38*, 79–91. https://doi.org/10.1016/j.immuni.2012.12.001.

57. Goldmann, T., Wieghofer, P., Müller, P.F., Wolf, Y., Varol, D., Yona, S., Brendecke, S.M., Kierdorf, K., Staszewski, O., Datta, M., et al. (2013). A new type of microglia gene targeting shows TAK1 to be pivotal in CNS autoimmune inflammation. Nat. Neurosci. *16*, 1618–1626. https://doi.org/10.1038/nn.3531.

58. Gee, J.M., Smith, N.A., Fernandez, F.R., Economo, M.N., Brunert, D., Rothermel, M., Morris, S.C., Talbot, A., Palumbos, S., Ichida, J.M., et al. (2014). Imaging activity in neurons and glia with a Polr2a-based and cre-dependent GCaMP5G-IRES-tdTomato reporter mouse. Neuron *83*, 1058–1072. https://doi.org/10.1016/j.neuron.2014.07.024.

59. Almeida, R.G., Czopka, T., Ffrench-Constant, C., and Lyons, D.A. (2011). Individual axons regulate the myelinating potential of single oligodendrocytes in vivo. Development *138*, 4443–4450. https://doi.org/10.1242/dev.071001.

60. Almeida, R.G., Williamson, J.M., Madden, M.E., Early, J.J., Voas, M.G., Talbot, W.S., Bianco, I.H., and Lyons, D.A. (2021). Myelination induces axonal hotspots of synaptic vesicle fusion that promote sheath growth. Curr. Biol. *31*, 3743–3754.e5. https://doi.org/10.1016/j.cub.2021.06.036.

61. Kwan, K.M., Fujimoto, E., Grabher, C., Mangum, B.D., Hardy, M.E., Campbell, D.S., Parant, J.M., Yost, H.J., Kanki, J.P., and Chien, C.-B. (2007). The Tol2kit: a multisite gateway-based construction kit for Tol2 transposon transgenesis constructs. Dev. Dyn. *236*, 3088–3099. https://doi.org/10.1002/dvdy.21343.

62. Berger, J., and Currie, P.D. (2013). 503unc, a small and muscle-specific zebrafish promoter. Genesis *51*, 443–447. https://doi.org/10.1002/dvg.22385.

63. Pittolo, S., Yokoyama, S., Willoughby, D.D., Taylor, C.R., Reitman, M.E., Tse, V., Wu, Z., Etchenique, R., Li, Y., and Poskanzer, K.E. (2022). Dopamine activates astrocytes in prefrontal cortex via α1-adrenergic receptors. Cell Rep. *40*, 111426. https://doi.org/10.1016/j.celrep.2022.111426.

64. Kingman, J.F.C. (1992). Poisson Processes (Clarendon Press). https://doi.org/10.1093/oso/9780198536932.001.0001.

65. Muggeo, V.M.R. (2003). Estimating regression models with unknown breakpoints. Stat. Med. *22*, 3055–3071. https://doi.org/10.1002/sim.1545.

66. Reddy, B.S., and Chatterji, B.N. (1996). An FFT-based technique for translation, rotation, and scale-invariant image registration. IEEE Trans. Image Process. *5*, 1266–1271. https://doi.org/10.1109/83.506761.

67. Song, L., Hennink, E.J., Young, I.T., and Tanke, H.J. (1995). Photobleaching kinetics of fluorescein in quantitative fluorescence microscopy. Biophys. J. *68*, 2588–2600. https://doi.org/10.1016/S0006-3495(95)80442-X.

68. David, H.A., and Nagaraja, H.N. (2004). Order Statistics (John Wiley & Sons).

69. Wang, Y., Wang, C., Ranefall, P., Broussard, G.J., Wang, Y., Shi, G., Lyu, B., Wu, C.-T., Wang, Y., Tian, L., et al. (2020). SynQuant: an automatic tool to quantify synapses from microscopy images. Bioinformatics *36*, 1599–1606. https://doi.org/10.1093/bioinformatics/btz760.

70. Müller, M. (2007). Dynamic Time Warping. Information retrieval for music and motion, 69–84.

71. Krishna, K., and Murty, M.N. (1999). Genetic K-means algorithm. IEEE Trans. Syst. Man Cybern. B Cybern. *29*, 433–439. https://doi.org/10.1109/3477.764879.

72. Taha, A.A., and Hanbury, A. (2015). Metrics for evaluating 3D medical image segmentation: analysis, selection, and tool. BMC Med. Imaging *15*, 29. https://doi.org/10.1186/s12880-015-0068-x.

73. Butler, R.W. (2007). Saddlepoint Approximations with Applications (Cambridge University Press). https://doi.org/10.1017/CBO9780511619083.

STAR★METHODS

KEY RESOURCES TABLE

REAGENT or RESOURCE	SOURCE	IDENTIFIER
Deposited data		
Raw data for Figures 2B, 2C, 3A, 3C, 5, and 6	This paper	https://dx.doi.org/10.17632/9f5myhx6jy
In vivo astrocytic calcium recording from mouse visual cortex (Figure 2A)	Wang et al.[14]	https://drive.google.com/file/d/1TjfFzlg_6BxsFX_l3-P92M5Rp_5j6wiM/view
Ex vivo astrocytic calcium imaging (Figure 3B)	Wang et al.[14]	https://drive.google.com/file/d/13tNSFQ1BFV__42TY0lZbHd1VYTRfNyfD/view
Calcium imaging of apical dendrites in mouse visual cortex (Figure S6E)	Gillon et al.[53]	https://dandiarchive.org/dandiset/000037/0.240209.1623
Calcium imaging in the parietal cortex of a mouse (Figure S7)	Giovannucci et al.[11]	https://users.flatironinstitute.org/~neuro/caiman_paper/K53.html
Experimental models: Cell lines		
Zebrafish:*Tg(mbp:memGCaMP7s; cryaa:mCherry)*	This paper	N/A
Mouse: *Tg GFAP-Cre* crossed with *Ai95(RCL-GCaMP6f)-D*	Garcia et al.[54] and Madisen et al.[55]	(RRID:IMSR_JAX:012886); (RRID:IMSR_JAX:024105)
Mouse: *Tg Cx3cr1-Cre/ERT2* crossed with *Polr2a(CAG-GCaMP5g-tdTomato)*	Yona et al.,[56] Goldmann et al.,[57] and Gee et al.[58]	(RRID:IMSR_EM:06350); (RRID:IMSR_JAX:024477)
Oligonucleotides		
Fyn-myr-fwd-/5Phos/CATGGGCTGT GTGCAATGTAAGGATAAA GAA GCAACAAAACTGACGGG	This paper	N/A
Fyn-myr-rev-/5Phos/CATGCCCGTCA GTTTTGTTGCTTCTTTAT CCTT ACATTGCACACAGCC	This paper	N/A
Recombinant DNA		
P5E-mbpa	Almeida et al.[59]	N/A
pME-GCaMP7s	Almeida et al.[60]	N/A
pME-memGCaMP7s	This paper	N/A
P3E-polyA; from tol2kit	Kwan et al.[61]	http://tol2kit.genetics.utah.edu/index.php/Main_Page
pDestTol2pA2-cryaa:mCherry	Berger and Currie[62]	Addgene #64023
Tg(mbp:memGCaMP7s; cryaa:mCherry)	This paper	N/A
Software and algorithms		
MATLAB	MathWorks	https://www.mathworks.com/products/matlab.html
AQuA2 (MATLAB version)	This paper	https://github.com/yu-lab-vt/AQuA2
AQuA2 (Fiji version)	This paper	https://github.com/yu-lab-vt/AQuA2-Fiji
AQuA2 (Cloud version)	This paper	https://yulab.vt.domains/AQuA2
AQuA	Wang et al.[14]	https://github.com/yu-lab-vt/AQuA
Begonia	Bjørnstad et al.[16]	https://github.com/GliaLab/Begonia
CaImAn	Giovannucci et al.[11]	https://github.com/flatironinstitute/CaImAn
suite2p	Pachitariu et al.[12]	https://github.com/MouseLand/suite2p

EXPERIMENTAL MODEL AND STUDY PARTICIPANT DETAILS

Animals

Zebrafish (Ahrens lab)

Experiments were conducted according to the guidelines of the National Institutes of Health and were approved by the Standing Committee on the Use of Animals in Research at Harvard University. Animals were handled according to IACUC protocols 22-0216 (Ahrens lab). We did not determine the sex of the fish we used since it is indeterminate at this age. Fish were raised in shallow Petri dishes and fed ad libitum with paramecia after 4 dpf. Fish were raised on a 14 h:10 h light:dark cycle at around 27°C. All experiments were done during daylight hours (4–14 h after lights on). All protocols and procedures were approved by the Janelia Institutional Animal Care and Use Committee.

Zebrafish (Lyons lab)

Adult zebrafish were housed by the bioresearch and veterinary service at the Queens Medical Research Institute at the University of Edinburgh. Studies were carried out with the approval of the UK home office and according to its regulations (project license PP5258250). Adult animals were maintained at a 14-h day and 10-h night cycle. Embryos were housed at 28.5°C in 10 mM HEPES buffered E3 medium. Zebrafish embryos were imaged at 3 dpf, before the onset of sexual differentiation. In this study the transgenic (Tg) *mbp:memGCaMP7s* was used.

Mouse (Nimmerjahn lab)

All mouse procedures followed the National Institutes of Health (NIH) guidelines and were approved by the Institutional Animal Care and Use Committee (IACUC) at the Salk Institute under protocol number 13-00022. Mouse strains used in this study included *GFAP-Cre* (RRID: IMSR_JAX:012886), *Ai95(RCL-GCaMP6f)-D* (RRID: IMSR_JAX:024105), *CX3CR1-Cre/ERT2* (RRID: IMSR_EM:06350), and *Polr2a(CAG-GCaMP5g-tdTomato)* (RRID: IMSR_JAX:024477) mice. All mice were on a C57BL/6 J background. Mice were group-housed, provided with bedding and nesting material, maintained on a 12-h light-dark cycle in a temperature (22±1°C) and humidity-controlled (45–65%) environment, and provided with food and water ad libitum. The experiments involved 6- to 12-week-old heterozygous male and female *GFAP-GCaMP6f* mice (Figures 2C and 5) and 15- to 16-week-old male and female *CX3CR1-GCaMP5g-tdTomato* mice (Figure 6A). Cre-mediated DNA recombination in Cre/ERT2 mice was induced following established protocols. Briefly, tamoxifen (T5648, Sigma-Aldrich) was diluted in corn oil (C8267, Sigma-Aldrich) and injected intraperitoneally at 100 mg per kg (body weight) once a day for five consecutive days, followed by imaging ~3–5 weeks after the final injection. Sex as a biological variable was not considered in the research design and analyses, as the study's primary goal was to demonstrate the analysis approach's technical capabilities. Experimental mice used in individual experiments typically originated from different litters. Mice had marks for unique identification. No criteria were applied to allocate mice to experimental groups.

Mouse (Poskanzer lab)

All experiments were done in *Mus musculus* with a Swiss or C57BL/6J genetic background. The mouse protocols were approved by the University of California, San Francisco Institutional Animal Care and Use Committee (IACUC). Mice were housed on a 12:12 light-dark cycle and were provided food and water ad libitum. Approximately equal numbers of male and female mice were used in experiments.

Transgenesis

mbp:memGCaMP7s; cryaa:mCherry transgenic line

To generate a *Tg(mbp:memGCaMP7s; cryaa:mCherry)* transgenesis construct, we first created a tol2kit-compatible middle-entry vector containing the coding sequence for the membrane-tethered *memGCaMP7s*, *pME-memGCaMP7s*. To do this, we digested our previously generated plasmid *pME-jGCaMP7s*[60] (containing an untethered, cytoplasmic *GCaMP7s* coding sequence) at the start codon with NcoI-HF enzyme (GCCAC**CATG**G, NcoI recognition sequence underlined, start codon in bold, NcoI-HF from New England Biolabs). Into this digested vector we then ligated two annealed primers, Fyn-myr-fwd and Fyn-myr-rev, phosphorylated at the 5' end (from IDT DNA Technologies), which encode the myristoylation motif of human Fyn kinase flanked by overhanging NcoI-compatible ends. The sequence for this plasmid was verified by Sanger sequencing.

To generate the final Tol2 expression construct *Tg(mbp:memGCaMP7s; cryaa:mCherry)*, we then recombined 10fmol of the following entry vectors: previously described 5'-entry vector 5E-mbp[59] *ME-memGCaMP7s*, and 3E-polyA from the tol2kit[61]; and 20fmol of destination vector *pDestTol2pA2-cryaa:mCherry*[62] (Addgene #64023), using LR Clonase II Plus. 3-4 clones were tested for correct recombination by restriction enzyme digestion.

To establish a stable transgenic line, we injected 5pg of *Tg(mbp:memGCaMP7s; cryaa:mCherry)* plasmid DNA with 50pg tol2 transposase mRNA into wild-type zebrafish eggs at the one-cell stage. This yielded *memGCaMP7s*-expressing oligodendrocytes in injected embryos, which were then raised to adulthood. Founders were identified by screening their F1 offspring for germline transmission using the *cryaa:mCherry* marker.

GRAB-ATP *virus injections*

Viral injections were done in P0-3 pups. For all injections, pups were anesthetized on ice for 3 minutes and then positioned on a digital stereotax. Using a microinjection pump (UMP-3, World Precision Instruments), a mixture of *AAV9-GfaABC1D-GrabATP*1.0 with dye (2μl virus + 0.5μl Fast Green dye; virus titer 1.78x 10^13 VG/mL) was injected at four injection sites in a 2×2 grid over the visual cortex. The first injection coordinate was 0.8-0.9mm lateral and 1.5-1.6mm rostral from lambda, and each site was separated by 0.8mm. At

each site, 20-30nl of the virus was injected at two z-depths (0.1 and 0.2mm below the skull) at 3nl/s. Pups recovered from anesthesia on a heating pad before being returned to their home cage.

METHOD DETAILS

Data collection

Public datasets

The *in vivo GCaMP6f* dataset used in Figure 2A, and *ex vivo GCaMP6* dataset used in Figure 3B are public datasets recording the astrocytic calcium signals of the mouse brain slice. Their description can be found in the AQuA paper[14] and they can be downloaded from example datasets in https://github.com/yu-lab-vt/AQuA. Since the field of view (FOV) in the *in vivo GCaMP6f* dataset is rotated, we performed preprocessing and cropping to correctly orient the FOV.

The *GCaMP6f* calcium imaging used in Figure S6E, is a public dataset recording the signals on the apical dendrites in the mouse visual cortex. Its description was detailed by Gillon et al.,[53] and it can be downloaded from https://dandiarchive.org/dandiset/000037/0.240209.1623).

The multi-session *GCaMP6f* imaging data used in Figure S7 is a public dataset recording the neuronal calcium signals of the mouse parietal cortex. Its description can be found in the CaImAn paper[12] and it can be downloaded from https://users.flatironinstitute.org/~neuro/caiman_paper/K53.html.

Zebrafish whole-brain imaging (Ahrens lab)

Zebrafish whole-brain recordings were captured using a custom light sheet microscope with adjustable z resolution and consistent x and y resolutions of 0.40625um/px, as described by Mu et al.[33] Dual-color recordings involved simultaneous scanning at wavelengths of 488 nm and 561 nm, resolution of 2048 x 2048 pixels, with images separated using a dichroic mirror and captured on an Orca Flash 4.0 v2 camera. The detection objective was a 16x/0.8NA lens.

During experiments, paralyzed zebrafish performed fictive swimming in a VR environment, with the drifting gratings providing visual feedback, as shown in Figure 4. For the experiment in Figure 4, green and red calcium signals were expressed in neurons and astroglia using *Tg(ELAVL3: GCaMP7f)* and *Tg(GFAP: jRGECO1b)*, respectively. Caffeine 1mM was added in drug state. The frame rate was 1.41 Hz, with 10um per plane resolution, and 26 planes were collected. For the experiment in Figure 6D, the green NE signal and red astroglial calcium signal were expressed using *Tg(ELAVL3: GRABNE)* and *Tg(GFAP: jRGECO)*, respectively, in an open-loop setting with no visual feedback provided regardless of swim commands collected. The frame rate was set at 4.5 Hz. One suction electrode (~60 um inner diameter) filled with external solution, was placed over the dorsal side of the fish's tail and attached with gentle negative pressure. The voltage signal recorded by this tail was amplified and filtered (band-pass 300 Hz–3 kHz) with a MultiClamp 700B amplifier. This signal was then smoothed through convolution with an exponential filter and used as the 'swim signal'.

Mouse spinal recordings (Nimmerjahn lab)

Mouse spinal cord imaging was performed as previously described. Briefly, animals were implanted with a spinal and head plate under general anesthesia approximately one week before laminectomy and received Buprenorphine ER/SR (0.5 mg/kg) to minimize post-operative pain.

For intralaminar imaging through a dorsal glass window (Figures 2C and 6A), a laminectomy (2 mm wide × 4 mm long) was performed at the T12-T13 vertebra level, corresponding to spinal segments L3–L5. The dura mater overlying the spinal cord was kept intact, and a custom-cut #0 coverslip was used to seal the laminectomy, creating an optical window for imaging.

For translaminar imaging through an implanted glass reflective microprism (Figure 5), a 0.7 mm × 0.7 mm × 0.7 mm microprism with aluminum-coated hypotenuse (cat. no. 4531-0021; Tower Optical) was UV-cured (NOA 81; cat. no. 8106; Norland Products Inc.) to a custom-cut #0 coverslip matching the intended laminectomy size (3 mm wide × 4 mm long). A laminectomy (3 mm wide × 4 mm long) was performed at the T13-L1 vertebra level, corresponding to spinal segments L4–L6. Using a dissecting knife (cat. no. 10055-12; Fine Science Tools) attached to a stereotactic arm, a small incision was made 0.7 mm lateral to the central vein's center, coinciding roughly with the interface between the dorsal root ganglia (DRG) and spinal white matter in adult mice. The incision extended 0.7 mm in the rostrocaudal direction and 0.7 mm in depth, matching the microprism dimensions. No spinal cord tissue was removed. No blood exuded from the incision site upon retraction of the dissecting knife. The microprism implant was positioned above the incision site and slowly lowered until fully inserted (~0.7 mm depth). Excess fluid was removed using sterile absorbent paper points (cat. no. 50-930-669; Thermo Fisher Scientific). The implant was affixed to the surrounding bone with instant adhesive (cat. no. 3EHP2; Grainger).

Fluorescence image data were acquired with a wearable multi-color microscope (Figure 5) or macroscope (Figures 2C and 6A) using 473 nm excitation by a fiber-coupled DPSS laser. For imaging through the dorsal optical window (Figures 2C and 6A), using the wearable macroscope on freely behaving mice (16" x 16" open field), the typical average light power at the tissue surface was <250 μW mm−2. For imaging through the implanted microprism (Figure 5), using the multi-color microscope on focally restrained mice, 275-325 μW mm−2 was used. Translaminar image data were acquired four weeks after microprism implantation and at around 75 μm focal depths from the vertical microprism-tissue interface, where 0 μm was defined as the point when cells or blood vessels first came into focus. Our recordings showed no signs of phototoxicity at the specified light powers, such as a gradual increase in baseline fluorescence, lasting changes in activity rate, or blebbing of labeled cells. All data were acquired at the image sensor's full

resolution (1280 × 960 pixels) and maximum frame rate (~45 Hz). The image data were preprocessed as previously described, including illumination correction, background subtraction, and image registration. In a subset of recordings (Figures 2C and 5), mechanical stimuli were delivered to the animal's tail using a rodent pincher system (cat. no. 2450; IITC Life Science, Inc.). Pinch pressures were applied in the dorsoventral direction approximately 6 mm from the base of the animal's tail. Synchronously acquired analog data included the pressure sensor output from the rodent pincher system and the on-off TTL signal of the wearable microscope's light source, which were recorded at 1 kHz using DAQExpress 2.0 software (National Instruments). Pinch application and mouse behavior were also recorded on a video camera (≥20 Hz; Stingray F-033, Allied Vision Technologies) using AVT SmartView software (v1.11). To synchronize imaging with video data, we placed a near-infrared LED within the video camera's FOV, triggered from the microscope's light source drive signal (TTL pulse). The video data were cropped to the LED-on period and scored manually regarding mouse motor activity, pinch onset, and offset.

Zebrafish oligodendrocyte data (Lyons lab)

In the experiment depicted in Figure 6B, calcium in oligodendrocytes of zebrafish was expressed around the membrane using the *Tg(mbp:memGCaMP7s)*. The expression was recorded using an LSM880 confocal microscope operating in Airyscan fast mode, with a 20x water immersion lens. The zebrafish were then subjected to imaging for a total of 300 frames and 10 stacks. The acquisition frequency was set at 0.85 Hz, and the resolution was 0.0595μm per pixel. Then the data underwent several processing steps, including Airyscan processing, maximum intensity projection, and registration using turbo reg. The final processed data had dimensions of 2028 pixels x 248 pixels x 300 frames.

Mouse visual cortex recording (Poskanzer Lab)

In the experiment depicted in Figure 6C, acute coronal slices from the visual cortex (300um thick) were collected from P28-42 mice, as described previously by Pittolo et al.[63] All imaging was done at room temperature on a custom 2P microscope using a 920 nm laser, 525/50 emission filter, 256×256 pixel resolution, 20x objective with 1.0 N.A. (Olympus), a spatial resolution of 2.08um/px, and a frame rate of 5.62 Hz. Before 2P imaging, each slice was incubated for ~5 minutes in a 20mL recirculating standard artificial cerebrospinal fluid (ACSF) bath with 1uM TTX +/- 500nM POM1. Then, *GRAB-ATP* dynamics were recorded for 5 ~6 minutes. Before AQuA2 detection, all videos were smoothed along the z-axis by averaging every 2 frames.

In the experiment depicted in Figure 3C, imaging was performed as described in Reitman et al.[20] Briefly, a craniotomy was made over the right visual cortex and *AAV9.Syn.GCaMP6f*. WPRE.SV40 was injected through a glass pipette using a UMP3 microsyringe pump (World Precision Instruments) in order to express *GCaMP* in cortical neurons. A glass cranial window was implanted using a standard protocol and after at least 2 weeks for viral expression the animal was habituated on a custom-made circular running wheel. 2P imaging was performed in the visual cortex of the awake head-fixed animal using a Bruker microscope with a Nikon 16x, 0.8NA water-dipping objective with a 2x optical zoom (frame rate 1.7 Hz, field of view 412 x 412 um^2, resolution 512 × 512 pixels). A 950 nm excitation light with a 515/530 emission filter was used to image the neuronal *GCaMP*.

Synthetic data generation

For the synthetic data utilized in comparing the performance of AQuA and AQuA2, we employed randomly generated signals, each exhibiting varying SNR. For the synthetic data used to compare all the peer methods, we assumed all the pixels are with the same baseline value. We simulated datasets based on templates derived from real signals. To emulate authentic molecular spatiotemporal activity, we employ three distinct synthetic settings: unfixed size, unfixed location, and propagation. These datasets were generated under a consistent 10dB SNR. Consequently, across these scenarios, we evaluate performance under varying SNRs: 0dB, 2.5dB, 5dB, 7.5dB, 10dB, 15dB, and 20dB—resulting in a total of 7 distinct settings. Within each setting, we generate 4 diverse ground truth patterns and incorporate random noise for each pattern repeated 3 times.

Definition of SNR

We define the SNR of simulation using the following formula:

$$SNR = 20 \cdot \log_{10}\left(\frac{\textit{average signal intensity}}{\textit{noise standard deviation}}\right) \quad \text{(Equation 1)}$$

where the average signal intensity is the average intensity of all voxels belonging to the ground truth.

Synthetic data with low SNR

We simulated the synthetic data used in Figure 2B with size 500 pixels x 500 pixels x 500 frames, and a background image that changes gradually in the y dimension. We initially generated 100 signal centers at random positions, then applied Gaussian filters with uniformly distributed sizes on both spatial and temporal dimensions to them. As a result, those signals have radii ranging from 10 to 40 pixels, durations ranging from 10 to 20 time points, and centers with intensity ranging from 10% to 20% $\Delta F/F_0$. Afterward, we generated 10 signals using a similar approach in the same dataset, this time incorporating large Gaussian filters to simulate scenarios involving both large and small signals. The large signals have radii ranging from 40 to 80 pixels, durations ranging from 80 to 150 frames, and centers with intensity ranging from 30% to 40% $\Delta F/F_0$. Large signals are allowed to overlap with small signals, thus some small signals may be obscured. Finally, zero-mean Gaussian noise was added, with the variance of each pixel proportional to its baseline value. Combining with F_0, this provides a good approximation of Poisson noise according to the central limit theorem, which better reflects the characteristics of real data. A rough estimation of the SNR across the whole dataset is around 10dB.

Spatial template of signals in synthetic data

In the next six subsections, all the descriptions refer to the synthetic data used in Figure 3A. Given that ROI-based methods often demand users to define signal sizes, we utilized the regions of neuronal signals in mice as spatial templates, since the sizes of these signals are relatively consistent. These templates underwent processing involving morphological closing and dilation to fill gaps and refine boundaries. The templates are then randomly translated and rotated on a mask of size 512 pixels x 512 pixels, with the constraint that the closest distance between two ROIs should be larger than 5 pixels. On the final mask, there are 66 spatial templates, each with a size close to 20 pixels x 20 pixels.

Temporal template of signals in synthetic data

Similarly, ROI-based methods typically require the specification of the decay constant, which implies a fixed temporal pattern. To enable these methods to achieve relatively good performance, we adopted a signal template with a fast intensity increase and slow decay. The template reaches its maximum intensity of 1 at the third time point, with the first two frames reaching 0.4 and 0.8, respectively. Then the template presents a decay following the function $e^{-0.3t}$, where t is the time point after the peak. In general, if we consider a threshold of 20%, the temporal duration of the template is approximately 8 time points.

Ground truth data generation for synthetic data

We generated ground truth data of size 512 pixels x 512 pixels x 250 frames, using both spatial templates and temporal templates. For each spatial template, we uniformly distributed the peaks of the temporal pattern with a density of 0.04. To prevent signals from being too close for distinction, we retained only the first signal if two peaks were located within a time window of length 5 frames. Furthermore, to ensure that each signal is fully contained within the data, we do not allow the peaks to be in the initial or final frames. Following convolution with the temporal pattern at peak positions, each spatial template generates approximately 7-8 signal events. Furthermore, within the synthetic settings featuring variable sizes, diverse locations, and propagation, to guarantee the distinguishability of each ground-truth event, we prohibit signal centers from overlapping. The center, in this context, is defined as the portion exhibiting an intensity surpassing 50%.

For ground-truth labeling, a watershed algorithm based on the signal centers is used, with the constraint that voxels labeled as ground truth must have an intensity greater than threshold 0.2. In general, each synthetic data contains approximately 400-500 events.

Setting - unfixed size for synthetic data

To simulate potential changes in the size of signal events, we randomly altered the size of signals that correspond to the same spatial template while keeping their spatial center unchanged. A parameter called "size-change odds" controls the maximum size change, where a "size-change odds" of x means that the size can randomly vary from 1/x to x times its original size. Dilation and shrinkage have equal chances of occurring. The parameter varies from 1 to 2 in increments of 0.25. To achieve this, we generated a uniformly random variable between 1 and the parameter to represent the scale factor and another uniformly random variable between 0 and 1 to determine whether to dilate or shrink, with a threshold of 0.5. When testing the robustness under different SNRs, we set the "size-change odds" to be 1.5.

Setting - unfixed location for synthetic data

To simulate potential changes in the location of signal events, we randomly moved the position of signals that correspond to the same spatial template to a nearby region. The "location-change odds" parameter controls the maximum distance of translation, where an odds of x means that each signal event may be shifted within a range of 0 to x times the template diameter. The angle of translation is also random. In our setting, the parameter varies from 0 to 1 in increments of 0.2. To achieve this, we generated two uniformly random variables: one ranging from 0 to the parameter to represent the translation distance, and another ranging from 0 to 2π to represent the rotation angle. When testing the robustness under different SNRs, we set the "location-change odds" to be 0.4.

Setting - propagation for synthetic data

In our simulation of signal propagation, we generated signals with two distinct types of potential propagation: "move" and "grow", with equal chances of occurring. For the "move" propagation type, the signal patterns of pixels remain the same, but with a gradually changing delay among adjacent pixels. As a result, the signal appears to move to another position. Similarly, in the "grow" setting, there is also a gradually changing delay, but the signal patterns of pixels within the same event differ in duration. Pixels that produce signals earlier have a longer duration achieved by interpolation, and all pixels within the same event end at the same time point. Thus, such signals appear to grow into a larger region.

For both propagation types, we set the propagation speed to be the same, at 0.15 times the radius of the spatial template. This means that the patterns of pixels with a distance of 0.15 times the radius will be delayed by one time point. The propagation direction is fixed within one event but is selected uniformly from 0 to 2π. Additionally, all signals have the same propagation length, denoted by the "propagation frame" parameter in our setting. In our simulation, the parameter varies from 0 to 10 in increments of 2. When testing the robustness under different SNRs, we set the "propagation frame" to 4.

Synthetic data for comparison to correlation-based propagation analysis

Referring to Figure S1E, we generated synthetic data with dimensions of 500 pixels x 500 pixels x 100 frames, featuring a row-dependent waveform and column-dependent delay for each pixel. Before the peak, the waveform follows a Gaussian shape for each pixel, while post-peak, it exhibits an exponential decay with a parameter linked to the row. Typically, the duration of the curve ranges from 30 frames (at the top row) to 70 frames (at the bottom row). Concurrently, the curves of pixels experience varying delays across different columns, ranging from 0 (at the leftmost) to 20 (at the rightmost). Subsequently, noise was introduced to achieve an SNR

of 0 dB in the synthetic data. During the application of the correlation-based method, we utilized the average curve of the entire dataset as the reference curve.

AQuA2 event detection pipeline

AQuA2 utilizes the same processing pipeline for both 2D and 3D imaging data. For simplicity, this explanation focuses on 2D data, where the raw fluorescence data is represented as a three-dimensional matrix $F \in \mathbb{R}^{H\times W\times T}$. Here $x \in \{1,\cdots,H\}$ represents the horizontal spatial index, $y \in \{1,\cdots,W\}$ represents the vertical spatial index, and $t \in \{1,\cdots,T\}$ denotes the temporal index. H and W are the spatial dimensions, and T is the total number of time points.

The event detection pipeline of AQuA2 comprises five steps as shown in Figure 1B to detect signal events. Step 1 (Preprocessing) addresses experimental artifacts such as motion and photobleaching effects, removes baseline fluorescence, and estimates noise. Step 2 (Active region detection) applies a statistical test to identify active regions, each of which potentially contains activities. As each active region may encompass multiple signals, Steps 3 (Temporal segmentation) and 4 (Spatial segmentation) are designed to segment these regions temporally and spatially, ensuring that each resulting signal event contains only one peak and originates from a single source, in line with our event definition. Step 5 (Global signal detection) is optional and involves repeating Steps 2 to 4 to detect longer-duration signals but based on the processed ΔF after removing the previously detected signal events.

Additionally, there are many phased results in the detection pipeline, including active regions, seeds, subregions, super events, and events. Here, although we refer to them as regions later, we want to clarify in advance that they are all spatiotemporal components. The motivation and definitions of them will be given in corresponding steps.

Step 1: Preprocessing in AQuA2

The raw fluorescence F can be expressed as a mathematical equation $F = F_0 + S + N$, where $F_0 \in \mathbb{R}^{H\times W\times T}$ represents the baseline component, $S \in \mathbb{R}^{H\times W\times T}$ is the signal part, and $N \in \mathbb{R}^{H\times W\times T}$ denotes the noise. Since F_0 and N are not of primary interest, this step focuses on baseline estimation and noise modeling to improve conditions for signal detection. Then, with the noise model established, the fluorescence change $\Delta F \equiv F - F_0 = S + N$ is utilized in the subsequent analyses. Additionally, Step 1 also includes optional image registration and photobleaching correction to mitigate the impact of artifacts.

Baseline estimation: Instead of estimating the baseline from a single projection (like average projection or minimum projection) of the imaging data, AQuA2 accounts for potential temporal variations in the baseline to improve signal detection accuracy. With the assumption that baseline changes occur much more slowly than the target signals and the non-negative nature of signal activities, we model the baseline for each pixel using a piecewise linear function (Figure S1C): First, a moving average filter (typically with a window of 25 time points) is applied to reduce noise. Then, the time course for each pixel is segmented into equal-length intervals, with each interval exceeding the duration of target signals (default length: 200 time points). By connecting the minimum points in each segment, the influence of signals can be minimized and the slow-changing baseline variations can be captured. To offset the bias introduced by selecting the minimum points, a predetermined value is added later.

Noise modelling: After isolating the baseline F_0, only two components remained, that is $\Delta F = S + N$. To correctly identify the signals, noise distribution should be well estimated. Many methods[11,13] often assume that the noise distribution is independently and identically Gaussian, estimating a single noise standard deviation for the entire dataset. However, this assumption may not accurately reflect the actual noise characteristics. Fluorescence recordings, as an optical process, produce intensity values F that follow a Poisson distribution, meaning the noise variance differs based on the expected value. Additionally, according to the central limit theorem, when the photon count is sufficiently large, the Poisson distribution can be approximated by a particular Gaussian distribution. In our model, F_0 and S account for the expected value, while N accounts for the variance. For simplicity, we assume the expected value at each pixel remains constant, since F_0 exhibits minimal variation and S is sporadic. Thus, N is modeled as independent and identically distributed zero-mean Gaussian noise at each pixel.

Since different pixels may have different noise variances, we first estimate the noise pixel by pixel. Recall that F is the summation of three components, directly computing the variance of pixel (x,y) using $var\{F(x,y,t)|t = 1\ldots T\}$ would lead to overestimation, as it would include the variances of F_0 and S. Instead, AQuA2 estimates the noise level by examining the difference between adjacent time points. This approach assumes that over two adjacent time points F_0 is almost constant and S is slowly changing, so their impacts are significantly reduced in the difference, allowing for a more accurate isolation of noise.

$$\widehat{\sigma}^2(x,y) = \frac{1}{2} mean_{t=2,\ldots,T}(F(x,y,t) - F(x,y,t-1))^2 \qquad \text{(Equation 2)}$$

where x, y represent the spatial coordinates and t denotes the time point position.

Due to the limited temporal length of each pixel and an insufficient number of samples, the noise estimation described above may not be accurate enough. To improve this, we leverage a key characteristic of the optical recording: the strong correlation between noise variance and the expected value.[64] The relationship between variance $\widehat{\sigma}^2(x,y)$ and the expected value $\mu(x,y)$ can be modeled as a piece-wise linear function. Through this way, the information from all pixels can be integrated for enhanced estimation accuracy. Since we detect signals using the null hypothesis in subsequent analysis, we focus solely on the noise under the null hypothesis. Thus, assuming the signals are sporadic, we disregard the impact of the signal S on $\mu(x,y)$ and use the average projection of F_0, $mean\{F_0(x,y,t)|t = 1\ldots T\}$, as $\mu(x,y)$ at the pixel (x,y).

By plotting the estimated variance $\widehat{\sigma}^2(x,y)$ of all pixels from Equation 2 against their corresponding expected values $\mu(x,y)$ (Figure S1D), we observe that truncation at low expected values and saturation at high expected values introduce deviations from the expected linear relationship. Specifically, the slope at low expected values is slightly higher, while it becomes negative at high expected values. This occurs because intensity values above a certain threshold are capped, and values below zero are constrained. To account for this, we model the relationship using a three-segment piecewise linear function $f_{3-seg}(\cdot)$ (Figure S1D) with unknown break points to fit the relationship between $\widehat{\sigma}^2(x,y)$ and $\mu(x,y)$, which can be solved through a method proposed by Muggeo.[65] Then, a more reliable noise estimation $\sigma^2(x,y) = f_{3-seg}(\mu(x,y))$ can be computed and will be always used in the subsequent analysis.

Optional image registration: In fluorescent imaging data, jitter or drifting may occur in the recorded data. These artifacts often manifest as rigid translations, given the limited field of view in microscope. To mitigate motion artifacts, AQuA2 offers an option to apply the cross-correlation algorithm,[66] which aligns each frame by comparing its similarity to a reference image. Specifically, we solve the following optimization problem:

$$max_{\Delta x,\Delta y}\ sim(\Delta x,\Delta y)$$

$$sim(\Delta x,\Delta y) = \{I_1 * I_2\}(\Delta x,\Delta y) = \sum_x\sum_y I_1(x,y)\cdot I_2(x+\Delta x, y+\Delta y) \quad \text{(Equation 3)}$$

where Δx, Δy represents the translation in two dimensions, *sim* is the similarity measure, * denotes the convolution symbol, I_1 is the image to align, and I_2 represents the reference image. By default, the reference image is determined by averaging the first 10 frames.

This algorithm determines the optimal shift between two images by maximizing their similarity across all possible translations, where similarity is quantified by the convolution result, the summation of the products of corresponding pixel intensities from the two images. While it may appear necessary to iterate through every element in the image for each (Δx, Δy) to compute similarity, the convolution theorem in the Fourier domain offers a highly efficient solution.[66] Once the optimal shift is determined, rectifying the translation involves shifting the images in the opposite direction.

Optional photobleaching correction: Photobleaching is another potential artifact observed in fluorescent imaging data, wherein fluorescent probes gradually degrade due to exposure to excitation light, leading to a loss of fluorescence capability. The decay of fluorescence due to photobleaching is typically modeled using an exponential decay function.[67] AQuA2 offers two approaches to model photobleaching decay: (1) Global Modelling: The decay is modeled by fitting the average fluorescence intensity across all pixels to the exponential decay model $f(t) = ae^{-bt}+c$, where *a* represents the initial fluorescence intensity, *b* is the decay constant, and *c* accounts for the residual intensity; (2) Intensity-based Modelling: Acknowledging that the bleaching rate may vary across pixels with different intensities, an intensity-based correction method is employed. Specifically, pixels are clustered based on their baseline intensity, and then decay is modeled on the average curve of each cluster. In either approach, once the decay function is estimated, correction can be applied through dividing the fluorescence signal by the decay function.

Step 2: Active region detection in AQuA2

Following Step 1, AQuA2 obtains ΔF, which consists of signal *S* and noise *N*. In this step we want to detect spatiotemporal regions consisting of statistically significant (non-noise) voxels. As previously mentioned, noise is assumed to follow a zero-mean Gaussian distribution, and its variance at each pixel is estimated as $\sigma^2(x,y)$. Since signals are non-negative, AQuA2 uses hypothesis testing to assess the significance of intensity changes, with $\Delta F(x,y,t)/\sigma(x,y)$ serving as a z-score to represent the standardized fluorescence intensity. A higher z-score indicates a greater likelihood that the voxel contains a true signal. By applying a user-defined threshold (default set to 3, corresponding to a p-value 0.13% assuming the population follows a normal distribution), significant voxels are identified and aggregated as spatiotemporal regions, which are termed as **active regions**. User-provided prior knowledge about the target signals can also be incorporated. For example, information such as size (default set at 20 pixels), duration (default set at 5 time points), or signal shape (default set the circularity constraint at 0) are introduced as filters.

It is worth pointing out that the saturation in real data could lead to an underestimation of $\sigma(x,y)$ compared to the original noise variance, which affects $\Delta F(x,y,t)/\sigma(x,y)$. However, it does not directly lead to the conclusion that the signal detection power will increase due to a smaller value of $\sigma(x,y)$ than the original noise. When signals appear in regions approaching the saturation value, the signals exceeding the saturation value are clipped, leading to a corresponding decrease in $\Delta F(x,y,t)$. In our experience, the decrease of $\Delta F(x,y,t)$ is bigger than the decrease of $\sigma(x,y)$, resulting in a loss of detection power due to the saturation effect. Thus, experiments should be designed to minimize signal saturation when possible.

Step 3: Temporal segmentation in AQuA2

Recall that an event is defined as a spatiotemporally connected region characterized by fluorescent dynamics, exhibiting a single peak pattern and originating from a single source. In the preceding step, spatiotemporally connected regions potentially containing signal activities are detected. However, a single active region may contain multiple signals events, necessitating further segmentation to isolate individual events.

In Step 3, AQuA2 performs temporal segmentation on the active regions to obtain **super events**, each characterized by a single peak pattern, though potentially originating from multiple sources (Figure S1A). Following this, Step 4 further segments the super events into individual **events**, ensuring that each event's signals come from a single source (see Figure S1B).

The temporal segmentation in Step 3 involves the following procedures (Figure S1A): Firstly, we identify spatiotemporal regions with significant peak pattern within the active region as **seeds**; Then we segment the active region by expanding these seeds to larger regions, which are called **subregion**. Every subregion is guaranteed to contain only one peak pattern. However, over-segmentation is unavoidable due to intensity gap or texture. Adjacent subregions may share similar temporal patterns from one event. Hence, the third procedure is to merge similar subregions. After merging, signals exhibiting the similar peak pattern are gathered into the same spatiotemporal region, termed a **super event**. For convenience and without loss of generality, in this step, we work on the score map $\Delta F(x,y,t)/\sigma(x,y)$.

Seed detection: To ensure that each super event contains a single peak pattern, the active region is segmented by first identifying potential peak patterns. This is accomplished by assessing the temporal significance of candidate spatiotemporal regions selected using a top-down, multi-threshold, and multi-scale strategy.

The candidate region selection begins with a top-down multi-threshold strategy. This approach is chosen because regions under a low threshold may contain multiple peak patterns, while candidate regions above a high threshold are more likely to contain only one peak pattern.

For each threshold, the multi-scale strategy employed for region selection involves considering large scale yet weak signal regions, achieved through spatially downsampling operations. This aids in aggregating information over a broader field of view while enhancing SNR. Additionally, this strategy incorporates spatial morphology considerations. Among regions with identical temporal patterns and spatial extent, those with regular shapes are prioritized over irregular shapes, as they likely represent coherent biological structures. For instance, if two candidate spatiotemporal regions show the same temporal patterns and identical spatial size but differ in spatial morphology—one resembling a randomly generated winding line and the other having a regular shape like a square or circle—intuitively, the latter should hold greater significance. Through spatially downsampling operations, the intensity of the former is reduced by blending with non-signal pixels, while the intensity of the latter generally remains stable. Thus, this strategy also integrates morphology considerations. By default, AQuA2 considers scales of 2 × 2, 4 × 4, and 8 × 8.

The temporal significance of the candidate region obtained from the above strategy is then evaluated. Only if the significance is sufficiently high will the region be deemed to contain a peak pattern and thus be utilized as a seed. Notice that to ensure the singularity of the result's peak, if any seeds have already been detected within the selected candidate region (e.g., based on a higher threshold), AQuA2 will preserve these seeds without reassessment.

To measure the temporal significance of a candidate spatiotemporal region, AQuA2 avoids direct evaluation on its average curve of multiple pixels. This is because potential signal propagation and the presence of other signals could disrupt the significance assessment, making it difficult to establish a suitable time window for evaluation. Instead, AQuA2 measures the temporal significance at each pixel and combines the pixels' significances to evaluate the region's significance.

The significance of each pixel is evaluated by comparing the time window within the spatiotemporal region to its neighboring time points. Let the intensities of one pixel within the spatiotemporal region's time window be $(a_1,a_2,\ldots,a_n)$, and the intensities in the left and right neighboring time windows for of the same pixel be $(b_1,b_2,\ldots,b_m)$, where n and m are lengths of compared time windows (with $n = m$ by default), the contrast L can be calculated as follows:

$$L = \frac{a_1+a_2+\ldots+a_n}{n} - \frac{b_1+b_2+\ldots+b_m}{m} \quad \text{(Equation 4)}$$

Since candidate regions are selected through thresholding, the intensities of selected time window will always be larger than its neighbors, making the contrast L a biased measure that cannot be used to reliably evaluate temporal statistical significance. To address this, AQuA2 employs order statistic theory[68,69] to evaluate temporal significance of each pixel. This method assumes that the time points from two time windows are sampled from the same null hypothesis distribution, allowing for the calculation of the bias and variance of the contrast L based on the given order information. With the bias and variance of L determined, the significance of the contrast, and thus the temporal significance of a single pixel at that time window, can be derived as

$$z = \frac{L - \mu_L(J,H_0)}{\sigma_L(J,H_0)}, \quad \text{(Equation 5)}$$

where J is the relative ranking of intensities within the combined sample set from both time windows. For example, given intensities $b_2 < b_1 < a_2 < a_3 < a_1$, the relative order of (a_1,a_2,a_3,b_1,b_2) is $(5,3,4,2,1)$. H_0 represents the null hypothesis distribution (here we assume it is Gaussian distribution), $\mu_L(J,H_0)$ and $\sigma_L(J,H_0)$ denote the calculated bias and standard deviation under order J and null hypothesis H_0.

Given the temporal significances of pixels within the spatiotemporal candidate region, the next step is to aggregate these values to assess the significance of the entire candidate region. Since the time windows of the pixels may vary in length, duration-based weights are assigned to each pixel. For a region with K pixels, where the k th pixel has a temporal significance z_k and a corresponding time window of length n_k, the temporal significance of the candidate region is calculated as

$$z_{region} = \frac{\sum_{k}^{K} \sqrt{n_k} z_k}{\sqrt{\sum_{k}^{K} n_k}}, \quad \text{(Equation 6)}$$

Once a significance score exceeds a user-defined threshold (default set to 3.5 due to multiple testing), the candidate region is considered a seed. AQuA2 repeats the seed significance test across active regions, moving from high to low thresholds. If no seeds are detected in certain active regions, it suggests insufficient temporal significance, potentially indicating these active regions are false positives. Thus, the seed detection step also functions as a significance filter, removing temporally non-significant active regions.

Subregions obtained from seeds: If one active region contains multiple seeds, we segment the active region into "subregions". Each subregion is a grown region from a seed. We adopt a marker-controlled watershed algorithm on score map $\Delta F(x, y, t)/\sigma(x, y)$ due to its high efficiency and consistency with intuition. Notably, the watershed is performed in the spatiotemporal dimension. As a result, the entire active region is segmented into subregions, each containing a single seed and exhibiting one distinct peak pattern.

Merging: Considering the potential over-segmentation of the active region due to the texture or intensity gap within the fluorescent image, AQuA2 then employs a merging step to merge the neighboring subregions with a similar peak pattern, where the peak pattern is defined as the average intensity curve across all pixels within each seed, representing the temporal dynamics of signal intensity in that seed. The obtained results are termed **super events**.

Two rules for merging subregions are applied: First, spatially neighboring subregions with similar signal patterns should be merged to prevent over-segmentation (the similarity is introduced in the following); Second, temporally adjacent subregions with significant spatial overlap, measured by intersection over union (IoU), should remain unmerged to preserve temporal distinctness of events. Based on these rules, within one active region, AQuA2 greedily searches for spatially neighboring subregion pairs with the smallest temporal dissimilarity and merges them if their spatial overlap is tolerable, until the temporal dissimilarity exceeds a certain threshold.

To measure the temporal dissimilarity of two temporal patterns s_1 and s_2, which may have different time windows, we first extend both patterns to the same time window by padding with zeros. Then, dynamic time warping (DTW)[70] is used to find the best matches for each time point, aligning the time points by finding the optimal warping path for each time point in the extended time windows, allowing for the accurate comparison of temporal patterns despite possible variations in event duration. Given the obtained optimal warping path $P = \{(t_{s_1,i}, t_{s_2,i})\}$, where i is the index of the path, $t_{s_1,i}$ and $t_{s_2,i}$ represent the corresponding time points on s_1 and s_2, respectively. Thus, the temporal dissimilarity of s_1 and s_2 can be modeled as the average distance of each pair of corresponding time points:

$$d(s_1, s_2) = \frac{\sum_{(t_{s_1,i}, t_{s_2,i}) \in P} \left| t_{s_1,i} - t_{s_2,i} \right|}{|P|}, \quad \text{(Equation 7)}$$

where $|P|$ represents the size of the path P.

Such temporal distance $d(s_1, s_2)$ represents an absolute measure of the delay and shape difference between two temporal patterns. However, the significance of this distance varies with the duration of the patterns. If both patterns have short durations, the distance is more meaningful, while for longer durations, the same distance may indicate only trivial dissimilarity. Thus, a normalized distance considering the duration is then used as the dissimilarity measure.

$$D(s_1, s_2) = \frac{d(s_1, s_2)}{\min\left(T_{s_1}, T_{s_2}\right)}, \quad \text{(Equation 8)}$$

where T_{s_1} and T_{s_2} denote the lengths of original time windows for signal patterns s_1 and s_2.

Step 4: Spatial segmentation in AQuA2

As mentioned above, a super event may originate from multiple spatial sources, which contradicts our definition that each event should arise from a single source. Assuming that the signal source activates earlier than its surrounding pixels, AQuA2 performs spatial segmentation based on propagation information. This process involves two main steps (Figure S1B): propagation estimation and segmentation based on propagation. Final events will be detected.

Propagation estimation: Propagation estimation works on the temporal dimension of the super event to assess potential propagation or delay of each pixel. An intuitive approach is to identify the shift that maximizes the correlation between one reference and the pixel's curve, where the reference is usually defined as the average curve of the pixels in the super event. However, despite similarities in patterns, gradual deformation of the pattern within the super event can render propagation information unreliable, as depicted in Figure S1E.

Acknowledging the potential for deformation, we utilize alignment techniques to identify the optimal match or warping path between the pixel's curve and the reference (the average temporal pattern from the largest subregion). Among alignment techniques, AQuA2 employs joint alignment, which integrates structural information from the data and has demonstrated superior performance.[24] To enhance efficiency, joint alignment is solved using the BILCO algorithm,[24] developed by our team, which achieves a 10-fold

improvement in both time and memory usage. Once the optimal alignment warping functions are computed, the propagation information, including rising and decaying maps, can be visualized. Figures 4E, 5C, 6B, S1E, and S3B provide examples illustrating 50% rising maps, which display the time when pixels reach 50% of their peak based on propagation information.

Segmentation based on propagation: AQuA2 employs a multi-threshold strategy, which is executed in ascending order of 50% rising time, derived from propagation information, to identify potential source regions. The contrast in rising time map between the candidate region and its surroundings is then calculated to determine the source. The system offers sensitivity levels for signal source detection, with level 10 being the most sensitive and level 1 being the least.

There would be three cases in a super event: (1) No signal source region is detected. Then the super event is like a stationary signal activity and there is no need to segment. (2) Only one signal source is found. It denotes the super event comes from the same signal source, and thus still no need to segment. (3) Multiple signal sources are extracted, which means the super event is indeed coming from different sources. A marker-controlled watershed algorithm based on a rising map enables each spatial pixel to identify its nearest signal source according to rising time. Using the pixel labels, the super events are segmented into smaller spatiotemporal regions, referred to as events, each of which contains a single peak and originates from a single source, in accordance with our definition.

Step 5: Global signal detection in AQuA2

Global signal detection is an optional step aimed at identifying signals of extended duration that may have been obscured by shorter-duration signals detected in earlier stages (Figure S1F). For instance, if a signal component is the sum of 10 temporally disjoint local signals, each with a duration of 10, and a global signal in the same time window with a duration of 100, then the previous steps would only be able to detect the local signals with shorter durations. Global signal detection is specifically designed to capture such longer, obscured signals. This is accomplished by first removing the influence of local detections from ΔF (set the voxels of previously detected signals to NaN values then interpolate) then repeating Steps 2 to 4 with specific duration constraints that prioritize the identification of signals of extended duration. These constraints are tailored to capture signals with substantially longer durations compared to the shorter-duration signals detected previously.

AQuA2 CFU identification

With the intuition that spatial regions exhibiting repetitive spatiotemporal signals (events) indicate stable and biologically significant functional structures, we introduce the concept of a CFU. A CFU is defined as a spatial area generating a set of events with similar locations and morphologies. Events associated with a specific CFU share similar spatial territories, although not necessarily identical. The CFU concept combines the strengths of both ROI-based and event-based methodologies. It retains the notion of a ''region'' from ROI by grouping events with spatial consistency, while incorporating the flexibility of event-based methods to allow for some spatial variation among signals.

This concept serves as a more generalized version of ROI, offering increased flexibility. Unlike ROI, which is spatially static and confines signals to precisely the same territories, CFU acknowledges that signals may exhibit slight spatial variations. This flexibility is crucial for exploring functional units, as signals often do not maintain exactly the same territories in most data. Signals with higher intensity will span larger territories, while those with lower intensity will occupy relatively smaller areas. ROI-based methods may segment the union territory of these signals into multiple parts, identifying the overlapped region as a core ROI and the surrounding regions as independent ROIs, leading to the identification of false positive ROIs. The flexibility inherent in CFU positions it as a promising solution for exploring the functional units within such datasets.

CFU can be conceptualized as a collection of events characterized by consistent spatial patterns. Intuitively, identifying CFU can be framed as a clustering problem. Among classical unsupervised clustering algorithms, AQuA2 adopts a hierarchical clustering approach. This choice is motivated by the advantage of utilizing the interpretable largest allowable inconsistency as a hyperparameter, as opposed to relying on a predetermined cluster number - a challenging aspect to ascertain. For example, the unknown number of functional units makes methods like K-means[71] hard to apply, and there is the potential for false positive events to be clustered into distant regions. On contrary, the hierarchical clustering approach ensures that only signals with similar territories are clustered together. Even with potential false positive events, a filter based on the number of signals associated with CFU can effectively eliminate such instances.

Using the hierarchical clustering approach, the key issues in CFU identifications are how to define the spatial territory of one event and how to estimate the consistency/inconsistency between two territories. Inspired by the idea that in a given event, a pixel with a longer duration should hold greater importance, we use a weighted map, where weights are based on pixel durations, to represent the spatial territory (Figure S2A). For an event, let the set of pixels representing its spatial location be $M = \{(x_i, y_i)\}$, and the duration of i th pixel (x_i, y_i) within the event be denoted by n_i, the weight of i th pixel is defined as

$$w(x_i, y_i) = \frac{n_i}{max_i n_i}, \quad \text{(Equation 9)}$$

Using Equation 9, the weighted map of each event can be computed. Then, to estimate the consistency between two weighted maps, the weighted version of Jaccard similarity[72] is adopted:

$$Jaccard(w_1, w_2) = \frac{\sum_{(x_i,y_i)\in M_1 \cup M_2} \min\left(w_1(x_i, y_i), w_2(x_i, y_i)\right)}{\sum_{(x_i,y_i)\in M_1 \cup M_2} \max\left(w_1(x_i, y_i), w_2(x_i, y_i)\right)}, \quad \text{(Equation 10)}$$

where w_1 and w_2 are the weighted maps of event 1 and event 2, and $M_1 \cup M_2$ denotes the union set of pixel positions for these two events. This approach accommodates varying sizes of spatial territories and incorporates weight to provide an accurate measure of consistency. Its unweighted version, commonly known as IoU, is a standard metric for evaluating the match between two objects in computer vision tasks.

Once the crucial issues have been addressed, the clustering algorithm commences by treating each signal event as an individual group. It then iteratively clusters the most spatially consistent signal groups until the consistencies of all pairs are below the user-defined consistency. The consistency is set to 0.5 by default. Then an event number filter is applied to eliminate false positives, utilizing a default threshold of 3. For each remaining signal group, AQuA2 visualizes their average weighted map to showcase the CFU's position. Additionally, it captures the 50% rising times of the events within the group to construct the corresponding occurrence sequence for that CFU. These occurrence sequences play a pivotal role in quantifying the interactions between CFUs in subsequent analyses (Figure S2B).

Application scenarios and corresponding AQuA2 parameter settings

Here, we present the application scenarios along with the corresponding AQuA2 parameter settings.

Real application scenarios

Here, real-world application scenarios tested with AQuA2, along with other potential scenarios, are listed in Table S1. For the tested data, the parameter column provides the name of setting files saving corresponding parameter settings, which can be found in https://drive.google.com/drive/folders/107SF5V8fXxAsCxKw7l2N4BIo2cx4kUA-?usp=sharing. However, please note that even if the scenarios appear similar, the parameter settings may need adjustment based on experimental conditions, such as resolution or target signals, as these can lead to different outcomes.

Parameters for synthetic data

We apply the MATLAB version of AQuA2 to the synthetic data with the following parameters: We set the boundary removal "regMaskGap" to 0, minimum size "minSize" to 20, threshold "thrARScl" to 3, smoothing parameter "smoXY" factor to 1, baseline cut "cut" to 250, and minimum duration "minDur" to 2. All other parameters are set by default.

Settings for peer methods

In order to showcase the optimal performance of peer methods and ensure a fair comparison among them, we fine-tune their input parameters prior to application.

AQuA

We apply the MATLAB version of AQuA with the following parameters: We set "regMaskGap" to 0, "smoXY" to 1, "thrARScl" to 3, and "minSize" to 20. All other parameters are set by default. Notably, when comparing AQuA and AQuA2 in real applications, they shared the same basic parameter settings for a fair comparison.

Begonia

We apply the Begonia, a MATLAB package, to the synthetic data. The script code we used is the demo code for processing a single recording, with the following modifications: We let Begonia estimate the baseline using its default method rather than the 5th percentile of the first 100 frames. We set the min duration parameter "roa_min_duration" to 5, and the minimum size to be 20 to make it consistent with other event-based methods. The resultant activity regions (ROAs) are directly considered as events and compared with the ground truth.

CaImAn

We apply the newest Python version of CaImAn to the synthetic data. The script we use is modified based on "demos/notebooks/demo_pipeline.ipynb". The changes are listed below: Since there is no registration issue, we bypass the motion correction part. With the known temporal template of the signals, we specified the decay speed "decay_time" to 0.3. According to the spatial templates in our ground truth, we set the expected half size of neurons "gSig" to 15x15 and the half size of the patches to 50. The number of components per patch "K" is set to 10, while merging threshold "merge_thr" is specified as 0.5. Additionally, the amount of overlap between patches "stride_cnmf" is set to 10. To compare with ground truths, we extract the ROIs "estimates.A", their dFF "estimates.F_dff", and their decomposed spikes "estimates.S" to form spatiotemporal events.

suite2p

We apply the newest Python version of suite2p to the synthetic data. Since there is no registration issue, we set the parameter "do_registration" to False. The decay speed "tau" is specified as 0.3. Moreover, considering the spatial template we use, we set "spatial_scale" to 1 for good performance. Three features, ROIs' position "stat", ROIs' curves "F", and decomposed spikes "spks" are used to form spatiotemporal events.

QUANTIFICATION AND STATISTICAL ANALYSIS

Workstation configuration

All experiments were conducted on a workstation with Intel(R) Xeon(R) Gold 6140@2.30Hz processor, 128GB memory, running Windows 10 64-bit and using Microsoft VC++ compiler. No GPU was used. Two ROI-based methods were implemented in Python, while the other three event-based methods were implemented in MATLAB.

Event evaluation for ROI-based methods

AQuA2, AQuA, and Begonia are event-based methods that directly use the detected events as results, eliminating the need for further processing. In contrast, two ROI-based methods, CaImAn and suite2p, extract ROIs and their corresponding ΔF and decomposed spikes as results. Since ROIs are only spatial concepts, they cannot be used to compare with spatiotemporal ground truth events. Thus, we integrate spikes, ΔF, and ROIs into events for comparison.

To form spatiotemporal events based on ROIs, we first estimate the standard deviation of noise, denoted as σ, in the average ΔF curve of the target ROI. Time windows larger than 3σ are considered as candidates for containing signals, and each time window may include multiple signals. Decomposed spikes are then analyzed, with those of low strength treated as false positives and filtered out. The time windows are subsequently segmented based on the remaining spikes, with each of these spikes representing a single signal event. By combining the spatial ROI and segmented time windows, we can obtain signal events for performance evaluation.

Metrics for performance evaluation

To assess the accuracy of different detection methods, we employ two metrics: the weighted Intersection over Union (wIoU) and the F1 score. The wIoU evaluates the quality of detection at the voxel level while the F1 score measures the match relationship between detections and ground truths at the signal level.

wIoU

Motivated by the intuition that the brighter voxels should be assigned with larger weight, we use weighted IoU rather than the standard IoU to evaluate the quality of detection or the similarity between detection and ground truth. The weight of voxel v_k is defined as $w(v_k) = \max(c, I(v_k))$, where k is the index of voxel, c is one constant (set to 0.1) and $I(v_k)$ represent the intensity of voxel v_k before adding noise. The constant c is crucial, as it prevents overestimating the similarity when one detection contains ground truth but occupies an area several times larger.

With the assigned weight, the pairwise wIoU for i th detection D_i and j th ground truth G_j can be expressed as follows. One key advantage of this metric is its robustness: even when the ground truth is not perfectly defined, the score will exhibit only a negligible difference.

$$\mathrm{wIoU}(D_i, G_j) = \frac{\sum_{v_k \in D_i \cap G_j} w(v_k)}{\sum_{v_k \in D_i \cup G_j} w(v_k)}. \quad \text{(Equation 11)}$$

For each detected event D_i, we define the highest score among all pairs between it and all ground-truth events as wIoU_{D_i}, that is, $\mathrm{wIoU}_{D_i} = \max_j \mathrm{wIoU}(D_i, G_j)$. Similarly, for each ground-truth event G_j, the corresponding highest score is denoted as $\mathrm{wIoU}_{G_j} = \max_i \mathrm{wIoU}(D_i, G_j)$. We can then calculate an overall score by averaging the score of both detections and ground truths using the following formula:

$$\mathrm{wIoU} = \frac{\sum_i \mathrm{wIoU}_{D_i} + \sum_j \mathrm{wIoU}_{G_j}}{|D| + |G|}, \quad \text{(Equation 12)}$$

where D and G represent the detection set and ground truth set, and $|D|$ and $|G|$ denote the number of detections and ground truths, respectively.

The wIoU score ranges from 0 to 1, with a high score indicating a good match in voxel level between detections and ground truths.

F1 score

A pair of detection D_i and ground truth G_j matches when the following condition holds:

$$i = \mathrm{argmax}_k \mathrm{wIoU}(D_k, G_j), j = \mathrm{argmax}_k \mathrm{wIoU}(D_i, G_k), \quad \text{(Equation 13)}$$

That means that D_i/G_j is the most closely matched detection/ground truth pair among all other options at the voxel level for D_i and G_j. This definition helps to eliminate the impact of ground truth selection, as the match relationship remains unchanged regardless of whether voxels higher than 20% or 50% are selected as ground truth.

Let the number of matches be denoted as TP, the number of detections with no corresponding ground truth as FP, and the number of ground truths with no corresponding detection as FN. The F1 score can then be calculated as follows:

$$F1 = \frac{2TP}{2TP + FP + FN} \quad \text{(Equation 14)}$$

The F1 score ranges from 0 to 1, with a high score indicating a good match in signal level between detections and ground truths.

Interaction analysis of CFUs

Given that the curves of two biologically related CFUs may have different waveforms, baseline trends, or contamination from signals not originating from the measured CFU due to potential overlap, directly calculating the correlation coefficient using the two curves is not suitable. Instead, AQuA2 uses the occurrence sequences as features to analyze the interaction between two CFUs (Figures S2B and S2C).

We propose a statistical approach by examining the significance of co-occurrence between events in two sequences. Assuming the null hypothesis that each sequence follows a Poisson process with density λ, we can calculate the probability p that at least one event occurs within a time window of duration L.

$$p = P(N \geq 1) = 1 - P(N = 0) = 1 - e^{-\lambda L}, \text{where } P(N = k) = \frac{(\lambda L)^k}{k!} e^{-\lambda L} \quad \text{(Equation 15)}$$

To assess the interaction, we designate one sequence, say sequence 2 (with events), as the conditional sequence. We then create time windows centered around each event in sequence 2 and count how many of these windows contain at least one event from sequence 1. This count serves as a basis for evaluating dependency between the sequences. Assuming there are n events in the conditional sequence, m of whose time windows contain events from the other sequence, and that under the null hypothesis the probability of a time window containing at least one event is p, we can evaluate the significance of this dependency by:

$$\text{p-value}_{1|2} = \sum_{k=m}^{n} \binom{n}{k} p^k (1-p)^{n-k} = \sum_{k=m}^{\lambda_2 T} \binom{\lambda_2 T}{k} \left(1 - e^{-\lambda_1 L}\right)^k \left(e^{-\lambda_1 L}\right)^{n-k} \quad \text{(Equation 16)}$$

where λ_1 and λ_2 represent the densities of event sequences in CFU1 and CFU2, respectively. T denotes the sequence length. The p-value above is obtained from a statistical test based on the Binomial distribution (n, m, p).

Notably, two events in one sequence cannot correspond to the same event in another sequence. To prevent this, non-overlapping time windows are used when conditioned events occur too close to each other (Figure S2D). This may lead to different probabilities p for distinct conditioned events. In this case, simple Binomial cumulative probability cannot be applied. Instead, the saddle-point approximation method[73] is used to efficiently calculate the p-value.

During the analysis of the interaction between each pair of CFUs, AQuA2 will, by default, switch the conditional sequence (test twice) and gradually increase the length of the time window L from 0 until it reaches a user-defined value. The minimum p-value obtained above is then used as the final measure of significance to describe their dependency. Notably, the proposed methodology is directional, meaning that we can choose one specific sequence as the condition and assess dependency relative to this choice. This allows for testing the interaction by conditioning on either sequence, providing flexibility to determine dependency strength and direction. For instance, the sequence of can come from a CFU of interest, or an external stimulus sequence. Moreover, it is not necessary for the time window to be centered around the event, and the shifts of the windows are allowed.

The output features of AQuA2

The output features of AQuA2 can be divided into two categories: event-level features and CFU-level features. All the results can be obtained in the output "res.mat" file. Event-level features focus on the quantification of individual events, while CFU-level features describe the active functional units in the fluorescence imaging data.

Event-level features can be further divided into three classes: (1) Basic features of individual events, including voxel set, duration, area size, average curve of spatial footprint, average ΔF curve of spatial footprint, rising time, peak p-value, area under the curve (AUC), and others. These features serve as filters to select valuable signals and can also be utilized for statistical analysis, such as comparing changes in signal activity before and after the application of stimuli/drugs in controlled experiments. (2) Propagation-related features, including propagation speed, propagation map, and propagation trend in various directions. These describe the propagation information of events and can be used to uncover potential signal pathways. (3) Network features, which involve the distances between events and user-defined regions (e.g., cell regions or landmarks), as well as assessing the co-occurrence of events in spatial or temporal dimensions. The former reflects the association between specific regions and events, while the latter can be used to analyze the collective characteristics of events, such as signal bursts.

CFU-level features can also be categorized into three types: (1) Individual CFU information, including the spatial map, event sequence, average curve, and average ΔF curve. This is the result of CFU identification and can be utilized to visualize the active functional units in the data. (2) The dependency between every pair of CFUs, as well as the relative delay between two CFUs. This is the result of CFU interaction analysis. Users could utilize this information to investigate the interaction between CFUs. (3) The information of CFU groups, including CFU indexes and the relative delay of each CFU. This is the result of further postprocessing, which employs hierarchical clustering based on the dependency between CFU pairs. It can cluster CFUs into groups, show their relative order, and may unveil circuit pathways.

Supplemental figures

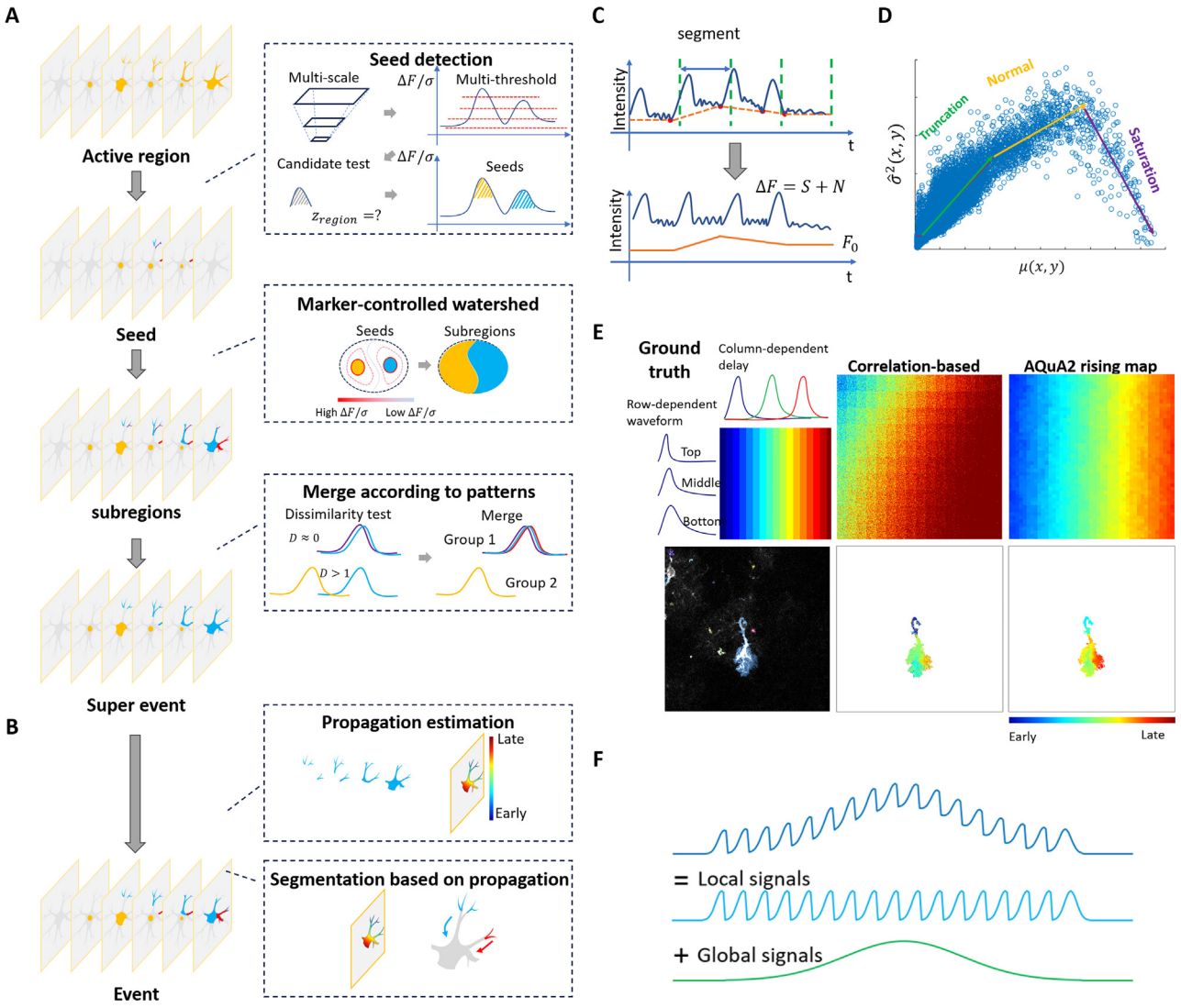

Figure S1. Supplementary diagrams for AQuA2 event detection pipeline, related to Figure 1

(A) Diagram illustrating temporal segmentation in the event detection pipeline.

(B) Diagram illustrating spatial segmentation in the event detection pipeline.

(C) Diagram illustrating baseline estimation.

(D) The noise variance estimated pixel by pixel versus expected value. Each blue circle represents one pixel/sample. The green, yellow, and purple line segments of the piecewise linear function represent the relationships under truncation, normal, and saturation cases, respectively. The noise variance is estimated based on Equation 2 in STAR Methods.

(E) A comparison between the correlation-based method and AQuA2 for propagation analysis. The top row displays simulation data featuring column-dependent delay and row-dependent waveform. The bottom row exhibits ex vivo astrocytic calcium recordings from mice. As demonstrated, the rising map generated by the correlation-based method tends to be noisy and prone to the influence of waveform, often leading to suboptimal outcomes. In contrast, AQuA2 employs joint alignment techniques, enabling it to deliver smooth, comprehensive, and precise information.

(F) Diagram illustrating the overlap of local and global signals. By default, AQuA2 detects local signals. Using the optional global signal detection step of AQuA2 mentioned in STAR Methods, global signals can also be detected.

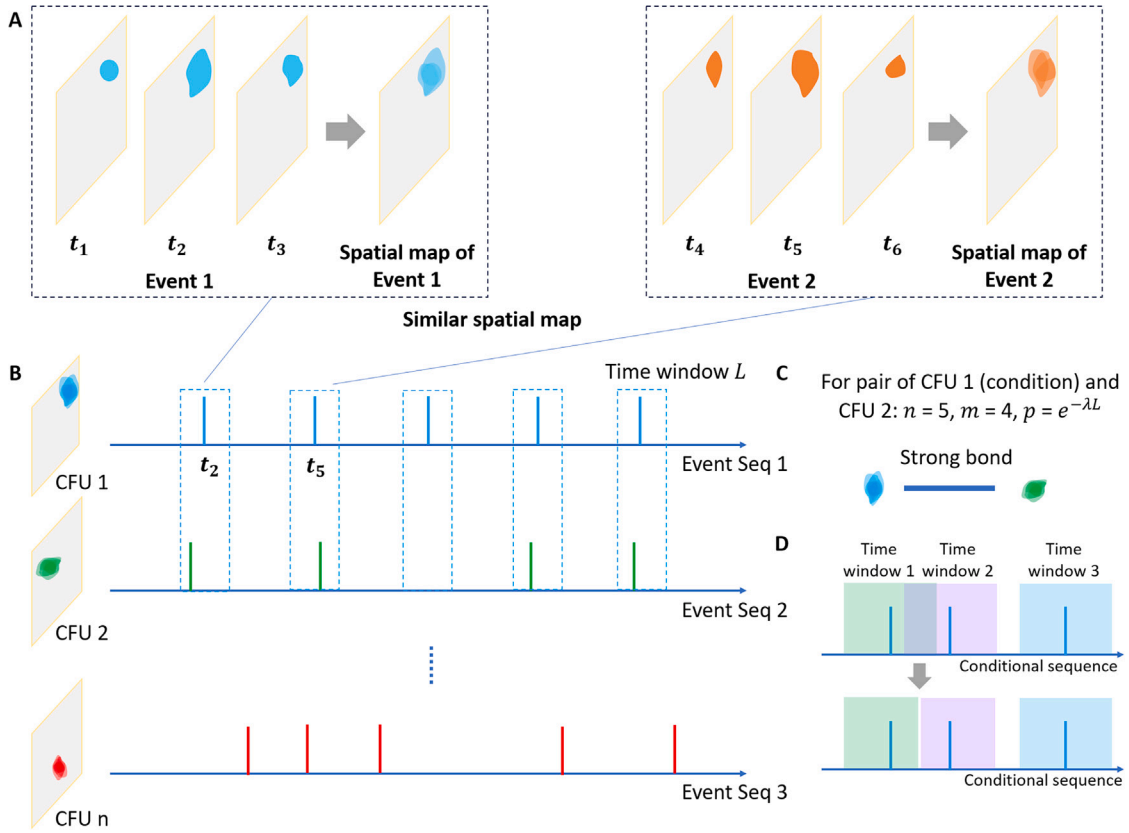

Figure S2. Supplementary diagrams for CFU, related to Figure 1

(A) Diagram illustrating the process of converting an event into a weighted spatial map.

(B) CFU region and its corresponding event sequence.

(C) Example pair of CFU 1 and CFU 2.

(D) Non-overlapping time windows are used to ensure that two events in a conditional sequence do not refer to the same event in another sequence.

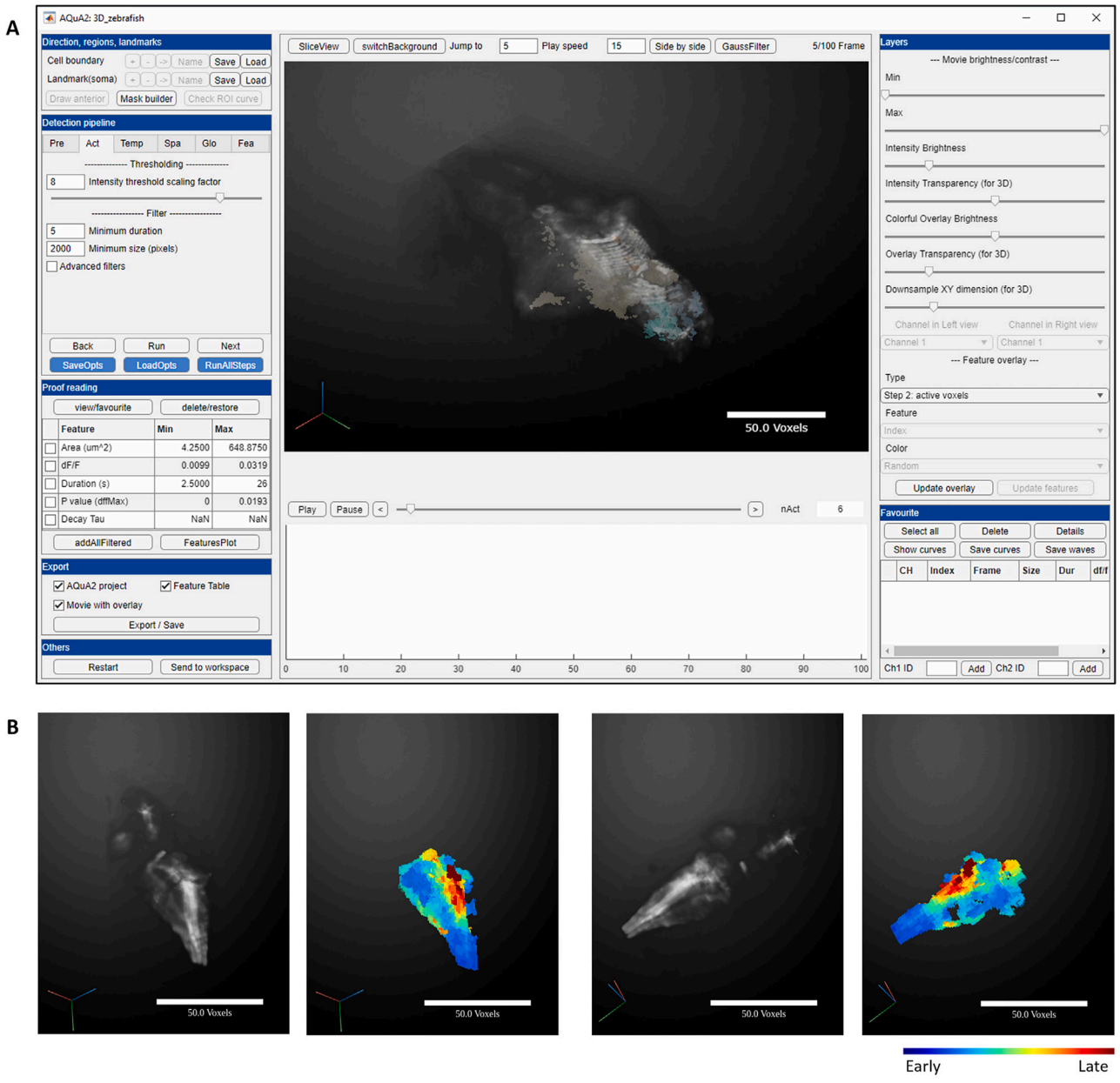

Figure S3. AQuA2 can be applied to 3D time-lapse imaging data, related to Figure 1

(A) AQuA2 GUI schematic diagram for 3D data. Each colored region represents one detected event.

(B) The signal propagation pattern was detected by applying AQuA2 on 3D astrocytic calcium recording in zebrafish expressing *Tg(GFAP: jRGECO1B)* under caffeine influence, with blue indicating early rising time and red indicating late rising time.

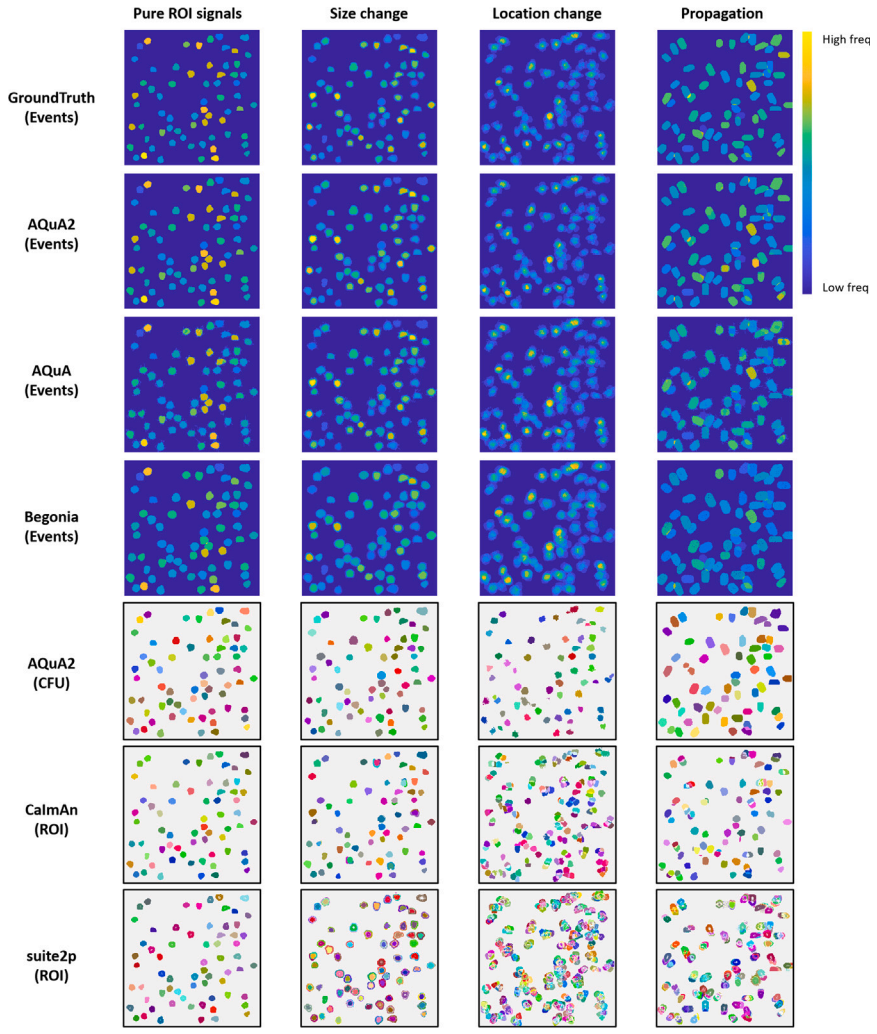

Figure S4. Detection results of peer methods on different experimental settings under 10dB SNR, related to Figure 3

From the first column to the fourth column, the experimental settings are pure ROI signals, signals with a size-change odd value of 2, signals with a location-change value of 2, and signals with a propagation frame value of 6, respectively. For the ground truth and event-based methods, we use the color to represent the frequency of events at each pixel (with dark blue and bright yellow representing the lowest and highest frequencies, respectively). For the ROI-based methods, we visualized each detected ROI by a colored region and compared the results of CaImAn and suite2p with the CFU results of AQuA2.

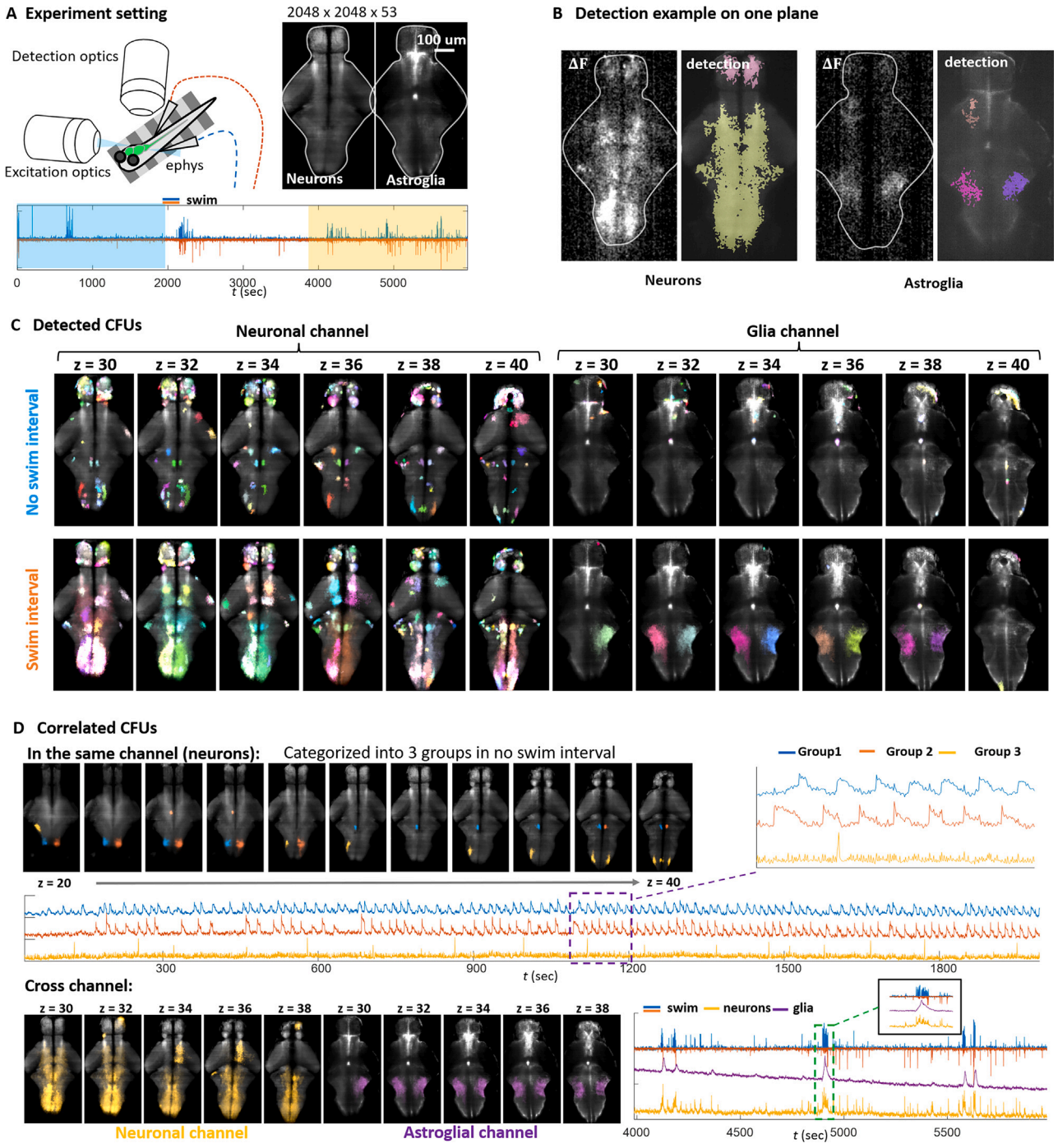

Figure S5. Application of AQuA2 on dual-color zebrafish recording, related to Figure 6

(A) Virtual environment for fictively swimming paralyzed fish. A custom light-sheet microscope was used to record neuronal calcium (*Tg(ELAVL3: GCaMP8f)*) and astroglial calcium (*Tg(GFAP: jRGECO)*). The frame rate is 3.01 Hz. Swim commands were detected by two probes. During the whole duration, two time windows were selected, labeled by blue and yellow masks, to observe the zebrafish signals in the non-swim interval or swim interval.

(B) Detection example on one plane. Each colored region represents one detected signal event.

(C) Detected CFUs of two intervals on different planes. Each colored region is one CFU.

(D) Obtained correlated CFUs. Top: three different CFU groups on different planes in non-swim intervals, with their average curves shown below. Bottom: correlated CFUs found in the cross channel of the swim interval with their average curves shown on the right.

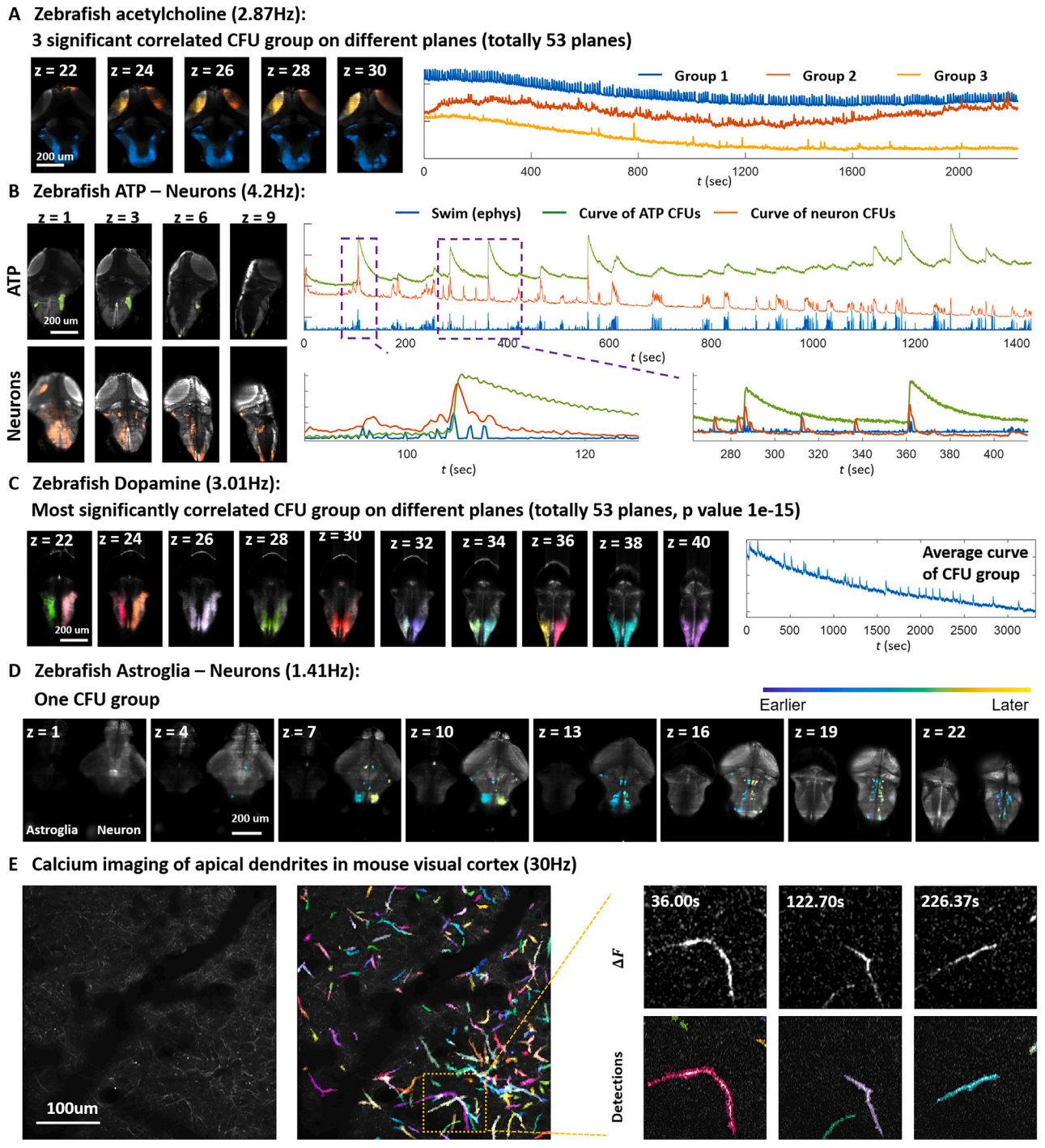

Figure S6. Supplementary applications of AQuA2 on more molecular signals and cell types, related to Figure 6

(A) Application of AQuA2 to identifying CFU groups on the zebrafish acetylcholine imaging. During the experiment, paralyzed zebrafish performed fictive swimming in a virtual-reality environment. Acetylcholine signals were expressed using *Tg(ELAVL3: AChSnFR)* and captured using a custom light-sheet microscope with a Z resolution of 5 μm/px and x and y resolutions of 0.40625 μm/px. The frame rate was set at 2.87 Hz. Each CFU group is labeled with a distinct color, with their average curve shown on the right. Each group shows a distinct signal pattern.

(B) Utilizing AQuA2 to identify correlated CFUs between the ATP channel and Neuron channel in zebrafish, despite waveform differences. ATP and neuronal signals were expressed using *Tg(ELAVL3:ATP)* and *Tg(ELAVL3:jRGECO)*, respectively, recorded by a custom light sheet microscope with a Z resolution of 10 μm/px and x-y resolutions of 0.40625 μm/px. The frame rate was set at 4.2 Hz. The average curves of CFUs for both channels (green and orange) are displayed on the right, alongside swim strength (blue). Zoom-ins of two time windows are provided. The obtained CFUs demonstrate a strong correlation with swimming behavior.

(legend continued on next page)

(C) Application of AQuA2 to identifying the most significant CFU group on different planes of zebrafish dopamine imaging. Each colored region represents one detected CFU, with the average curve of all these CFUs illustrated on the right. The dopamine was expressed using *Tg(GFAP: GRAB-DA)* and recorded by a custom light sheet microscope with a Z resolution of 4.9 μm/px and x and y resolutions of 0.40625 μm/px. The frame rate was set at 3.01 Hz. This application demonstrates AQuA2's capability to quantify dopamine activity.

(D) Application of AQuA2 to the CFU group identification and analysis in astroglia-neuron imaging in zebrafish. Astroglial calcium and neuronal calcium were expressed through *Tg(ELAVL3: GCaMP7f; GFAP: jRGECO1B)*. Each connected colored region is one CFU, and the color shows relative delay in this group. Using AQuA2, potential brain circuits can be found through CFU grouping.

(E) Application of AQuA2 to detect signals on *GCaMP6f* calcium imaging of apical dendrites in the mouse visual cortex (public data from https://dandiarchive.org/dandiset/000037/0.240209.1623).[53] From left to right, the visualization shows the average projection, CFU detection by AQuA2, and a comparison between ΔF and AQuA2 events within a small FOV. Each colored region represents a CFU or signal event. AQuA2 effectively identifies signals on these dendrites. The dynamic and overlapping spatial footprints are clearly observable, which hinders the application of ROI-based methods.

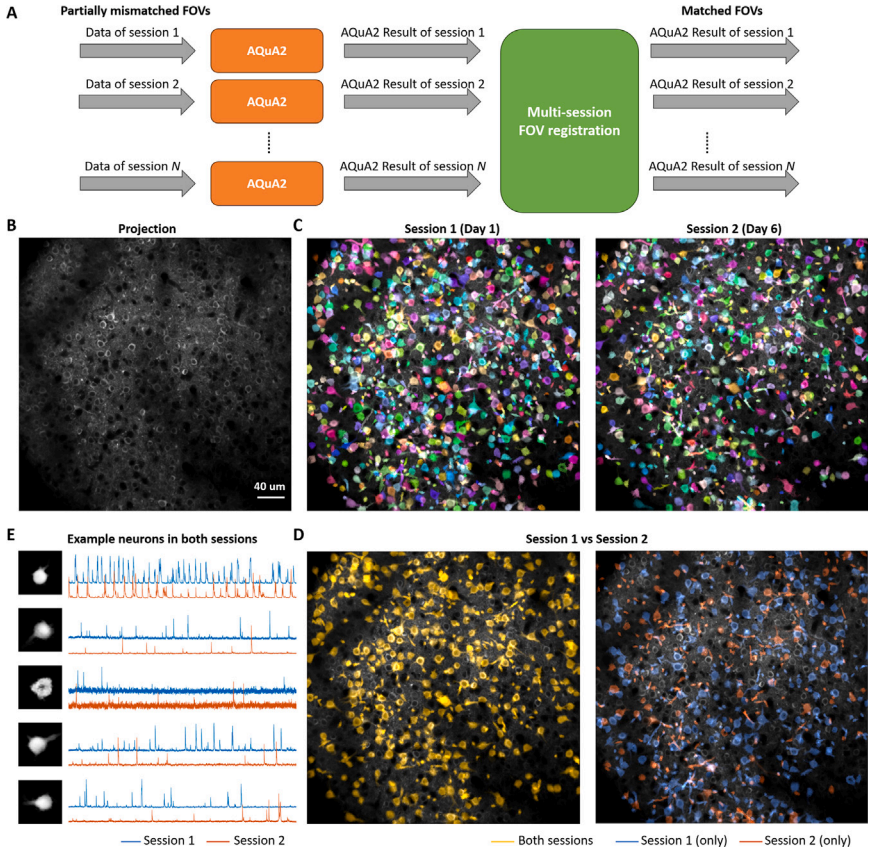

Figure S7. Supplementary applications of AQuA2 on multi-session imaging data, related to Figure 6

(A) Flowchart illustrating AQuA2's method for processing multi-session datasets. A script for multi-session FOV registration is available on GitHub.

(B) Median projection of *GCaMP6f* calcium imaging in the parietal cortex of a mouse (public data from https://users.flatironinstitute.org/~neuro/caiman_paper/K53.html), recorded over six days.[11]

(C) CFUs detected by AQuA2 across different sessions: Session 1 (first 15,000 images of the K53 dataset) and Session 2 (last 15,000 images). Each colored region represents an identified CFU.

(D) Comparison of CFUs between Session 1 and Session 2. CFUs present in both sessions are marked in yellow, while those unique to Session 1 are blue and those unique to Session 2 are red.

(E) Example neurons detected in both sessions, with their average fluorescence curves displayed on the right.